2018

Temporal and geochemical signatures in granitoids of northwestern Nevada: Evidence for the continuity of the Mesozoic magmatic arc through the western Great Basin

Kenneth L. Brown

William K. Hart

Richard J. Stuck

THE GEOLOGICAL SOCIETY OF AMERICA®

Temporal and geochemical signatures in granitoids of northwestern Nevada: Evidence for the continuity of the Mesozoic magmatic arc through the western Great Basin

Kenneth L. Brown[1], William K. Hart[2], and Richard J. Stuck[3]
[1]DEPARTMENT OF GEOLOGY AND GEOGRAPHY, WEST VIRGINIA UNIVERSITY, 330 BROOKS HALL, 98 BEECHURST AVE., MORGANTOWN, WEST VIRGINIA 26506, USA
[2]DEPARTMENT OF GEOLOGY AND ENVIRONMENTAL EARTH SCIENCE, MIAMI UNIVERSITY, 118 SHIDELER HALL, OXFORD, OHIO 45056, USA
[3]GREATER CINCINNATI WATER WORKS, 4747 SPRING GROVE AVENUE, CINCINNATI, OHIO 45232, USA

ABSTRACT

Granitoid magmatism in the Basin and Range Province of northwestern Nevada remains an important gap in our understanding of the along-strike variability of Mesozoic Cordilleran arc systems. We present a comprehensive investigation on a suite of intrusions within the Santa Rosa Range (SRR) and Bloody Run Hills (BRH) of northwestern Nevada. Petrography, whole-rock geochemistry, and zircon U-Pb geochronology indicate two distinct magmatic systems in the SRR: an older, mafic, and metaluminous pulse (Santa Rosa/Andorno [SRA] group—ca. 102–100 Ma) and a younger, felsic, and peraluminous pulse (Granite Peak/Sawtooth [GPS] group—ca. 94–92 Ma). Within the BRH to the south, the Flynn (ca. 105 Ma) and Bloody Run stocks (ca. 96 Ma) are compositionally similar to the SRA group. New Al-in-hornblende thermobarometry reveals emplacement paleodepths of ~5–10 km for the SRA group. Slightly deeper emplacement levels (~10.5–12 km) are inferred for the GPS group from structural relationships and metamorphic contact aureole assemblages. Elemental characteristics are correlated with whole-rock Sr and Nd isotope ratios, revealing higher $\varepsilon Nd_{(t)}$ (+0.8 to +2.5) and lower initial $^{87}Sr/^{86}Sr$ (0.7040–0.7054) in the older SRA group than the younger GPS group ($\varepsilon Nd_{(t)}$ = –3.2 to –1.5; $^{87}Sr/^{86}Sr_{(i)}$ 0.7056–0.7061). New zircon εHf isotope analyses reveal that with the exception of the Bloody Run stock (–0.4 ± 2.1), the SRA group has more primitive zircon $\varepsilon Hf_{(t)}$ values (+2.9 to +5.3) than the GPS group (+0.4 to –3.7). The systematic shift in whole-rock Sr and Nd isotope and zircon $\varepsilon Hf_{(t)}$ values with time suggests fundamental changes in the relative contributions of mantle and crustal sources. A comparison of published geochronology and geochemistry from regional intrusive suites confirms that SRR-BRH magmatism was coeval and geochemically similar to the larger Cordilleran batholiths, providing evidence for the continuity of the Mesozoic magmatic arc through northwestern Nevada.

LITHOSPHERE; v. 10; no. 2; p. 327–350; GSA Data Repository Item 2018123 | Published online 1 March 2018 https://doi.org/10.1130/L694.1

INTRODUCTION

The Sierra Nevada and Idaho batholiths represent a substantial volume of the Mesozoic magmatic arc record in the western United States and much attention has been given to their formation and evolution (e.g., Kistler et al., 1971; Kistler and Peterman, 1978; Bateman and Chappell, 1979; Hyndman, 1983; Wiswall and Hyndman, 1987; Kistler, 1990; Bateman, 1992; Coleman and Glazner, 1997; Gaschnig et al., 2010, 2011, 2017). However, relatively little is known about magmatism generated in the ~400 km gap between these larger batholith segments, making it difficult to evaluate along-strike spatio-temporal trends in crustal growth and arc processes. Although the Mesozoic history in the western Great Basin is often obscured by Cenozoic volcanism and faulting, reconnaissance-level studies have documented the significance of the exposed Mesozoic intrusive suites as well as explored their potential links to the larger batholith systems (e.g., Smith et al., 1971; Barton et al., 1988; Stuck, 1993; Van Buer and Miller, 2010; Brown et al., 2010, 2011; Brown and Hart, 2013). Despite these studies, the broader understanding for many of these intrusions remains limited to small numbers of samples aimed at identifying major crustal boundaries and economic mineral deposits (Zartman, 1974; Armstrong et al., 1977; Farmer and DePaolo, 1983; Solomon and Taylor, 1989; Elison et al., 1990; Wright and Wooden, 1991; Wooden et al., 1998, 1999; King et al., 2004; du Bray, 2007; Arehart et al., 2013). Many of the isolated intrusions within this region are emplaced in close proximity to important lithospheric boundaries that are interpreted to separate young accreted lithosphere from old Precambrian cratonic lithosphere (i.e., 0.706 isopleth). Therefore, detailed investigations of these isolated intrusive suites offer the potential to constrain the age, composition, and architecture of the underlying lithosphere.

This study focuses on one suite of isolated, but well-exposed, granitoid intrusions within the Santa Rosa Range (SRR) and Bloody Run Hills (BRH) of northwestern Nevada.

The SRR-BRH area is located at or near the convergence of several important regional geologic, geochemical, geophysical, and physiographic features within the North American Cordillera (Fig. 1). Specifically, it is located: (1) within the eastward-bend of the Mesozoic magmatic arc; (2) juxtaposed against the unextended volcanic plateaus of eastern Oregon along the northern boundary of the Great Basin; (3) within 100 km of major lithospheric boundaries identified using Sr, Nd, and Pb isotopes (e.g., Sr_i 0.706 isopleth); (4) near the northwestern end of the Northern Nevada Rift and other spatially associated economic mineral belts (e.g., Battle Mountain-Eureka and Carlin mineral trends); and (5) immediately southeast of the hypothesized inception of the Yellowstone hotspot track (McDermitt Caldera—ca. 16.5 Ma) (Fig. 1). A detailed investigation of the granitoid intrusions found within this area, therefore, permits several

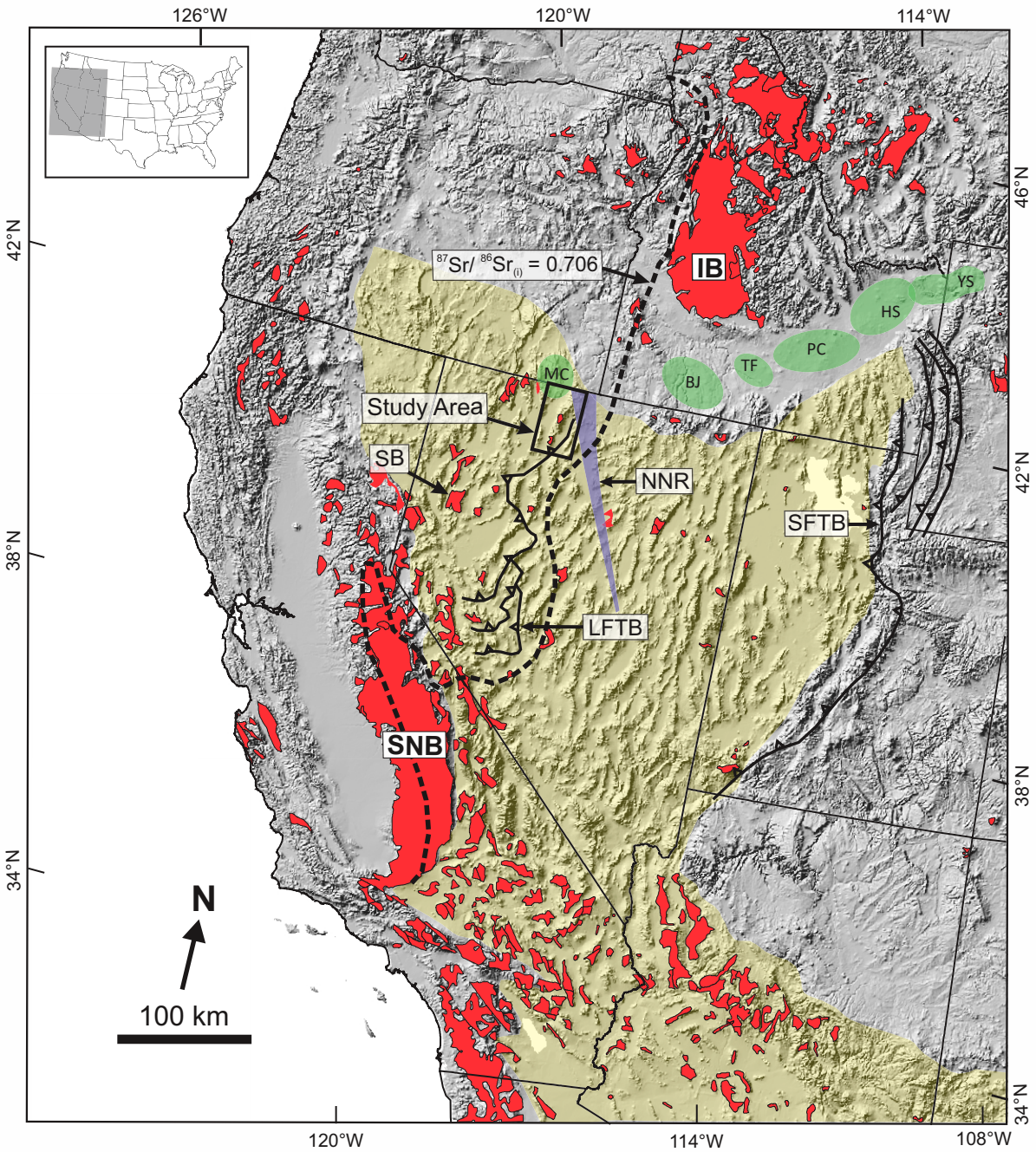

Figure 1. Shaded relief map of a portion of the western U.S. showing the distribution of granitoid intrusions (red shaded areas) as well as regional geologic, geochemical, and physiographic features: yellow shaded area—Great Basin physiographic province; IB—Idaho batholith; black dashed line—initial $^{87}Sr/^{86}Sr$ = 0.706 isopleth (after Kistler, 1990; Farmer and DePaolo, 1983); LFTB—Luning-Fencemaker Thrust Belt (after Wyld, 2002); purple shaded area—Northern Nevada Rift (NNR) (after Grauch et al., 2003); SB—Sahwave batholith (Van Buer and Miller, 2010); SFTB—Sevier Fold and Thrust Belt; SNB—Sierra Nevada batholith; green shaded ellipses—Yellowstone hotspot track; MC—McDermit; BJ—Bruneau–Jarbidge; TF—Twin Falls; PC—Picabo; HS—Heise; and YS—Yellowstone (after Brueseke et al., 2007).

key regional issues to be addressed that have important implications for the tectonomagmatic evolution and architecture of the North American Cordillera. These intrusions offer a more complete view of magmatism within the eastward-stepping portion of the Mesozoic magmatic arc and its continuity across the Basin and Range Province. Additionally, these intrusions also offer a unique window into the pre-Cenozoic history of this region, providing valuable constraints on the age, composition, and architecture of the underlying lithosphere prior to widespread Cenozoic volcanism (e.g., Steens flood basalts), the initiation of the hypothesized Yellowstone hotspot track, and Basin and Range extension. Therefore, to better characterize Mesozoic magmatism within this portion of Nevada, we present an integrated petrographic, geochemical, geochronologic, whole-rock Sr-Nd isotopic, and zircon Hf isotopic study.

GEOLOGIC BACKGROUND

Granitoid intrusions of Mesozoic age are common throughout western Nevada and are found along a general trend that extends from the northern Sierra Nevada Mountains to the Oregon-Idaho border. Although many of the granitoids are Middle to Late Cretaceous, older intrusions of Triassic and Jurassic age have also been identified (e.g., Stewart, 1980; Elison et al., 1990; Wyld and Wright, 2009). Located near the Idaho-Oregon-Nevada border, the SRR-BRH forms the northeasternmost limit of this belt of magmatism (Figs. 1 and 2). The SRR-BRH form two north-south–trending mountain ranges that are separated by a low pass (U.S. Highway 95); the SRR to the north and the BRH to the south (black box, Fig. 2).

Three early Mesozoic terranes are present in northwestern Nevada (Ciavarella and Wyld, 2008). From east to west, these include: (1) a continental shelf terrane; (2) a deep marine back-arc basinal terrane; and (3) an oceanic volcanic-arc terrane (Black Rock terrane: Figure 2; Wyld, 2002; Ciavarella and Wyld, 2008). Previous mapping and structural syntheses of the SRR-BRH area reveal that it is underlain by a deep marine back-arc basinal terrane, which is often referred to as the "Mudpile" (Lovelock assemblage of Oldow, 1984; Wyld, 2002) (Fig. 2). This basinal terrane, defined by Speed (1978), is a thick assemblage of Upper Triassic (Norian) deep-marine clastic strata (up to 6 km thick) consisting primarily

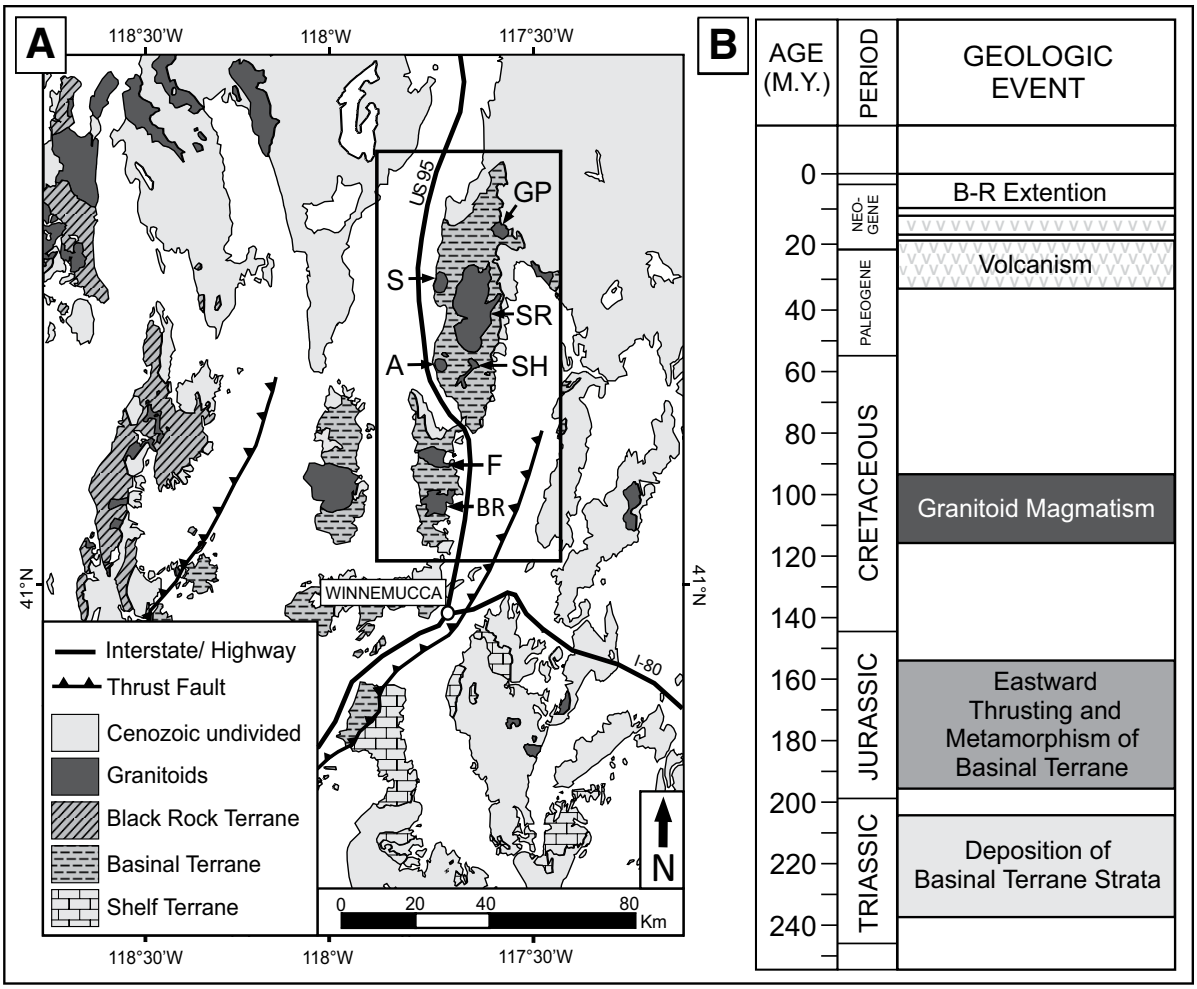

Figure 2. (A) Simplified geologic map of northwestern Nevada, showing the location of the Santa Rosa Range (SRR) and the Bloody Run Hills (BRH) (black box), terrane units, granitoid intrusions, undivided Cenozoic cover rocks, and Jurassic-Cretaceous thrust faults (after Compton, 1960; Stewart, 1980; Elison and Speed, 1989; Elison et al., 1990; Wyld and Wright, 2000; Wyld, 2002; Ciavarella and Wyld, 2008; Martin et al., 2010). A—Andorno stock; BR—Bloody Run stock; F—Flynn stock; GP—Granite Peak stock; S—Sawtooth stock; SH—Stone House stock; SR—Santa Rosa pluton. (B) Summary of major geologic events within this region (from Compton, 1960; Speed, 1978; Elison and Speed, 1989; Wyld et al., 1999; Wyld and Wright, 2001; Wyld, 2002; Wyld et al., 2003; Colgan et al., 2006; Brueseke et al., 2007; Brueseke and Hart, 2008; Martin et al., 2010).

of mudstones interpreted to have been deposited within a Triassic back-arc basin (Compton, 1960; Speed, 1978; Oldow, 1984; Wyld, 2002). These basinal terrane rocks were metamorphosed to low-greenschist grade slates and phyllites during regional east-vergent thrusting in Jurassic time along the Luning-Fencemaker fold-and-thrust belt (Wyld, 2002) (Figs. 1 and 2). Following regional metamorphism and thrusting, the basinal terrane was intruded by Cretaceous granitoids (ca. 116–93 Ma) (Colgan et al., 2006; Ciavarella and Wyld, 2008).

The next magmatic episode preserved in the SRR is represented by a suite of 35–19 Ma basalt through dacite lava flows that unconformably overlap the granitoid and metasedimentary basement (Brueseke et al., 2007, 2008; Brueseke and Hart, 2008). These relationships indicate that the granitoid intrusions and their surrounding host-rocks must have been exhumed prior to this period of regional volcanism (Brueseke and Hart, 2008).

Following a brief magmatic hiatus that marked a period of significant tectonic change (McKee et al., 1970), major outpourings of basaltic magma (Columbia River Basalt Group) initiated from an array of vent locations extending for over 1000 km from SE Washington to central Nevada (e.g., Carlson and Hart, 1988; Brueseke et al., 2007; Camp et al., 2013; Reidel et al., 2013). Accompanying the Steens Basalt component of this mafic magmatism in the Oregon-Idaho-Nevada region was substantial rhyolitic activity and local intermediate magma production, both well represented in the SRR (Brueseke et al., 2007, 2008; Brueseke and Hart, 2008; Brueseke and Hart, 2009). Commencing at ca. 10–12 Ma, the SRR was affected by modern Basin and Range faulting along its western and southern margins (Colgan et al., 2006).

FIELD OBSERVATIONS AND PETROGRAPHY

The four main intrusions in the SRR that were investigated as part of this study include: the Granite Peak stock, Sawtooth stock, Santa Rosa pluton, and the Andorno stock (Fig. 2). Smaller unnamed intrusive bodies are also present around the Santa Rosa pluton and in the southeast SRR. These smaller intrusions along with the Stone House stock were not examined in this study. To the south, two additional large intrusions are found in the BRH: the Flynn stock, and the Bloody Run stock (Fig. 2).

These intrusions, and their wall-rock relations, were first studied in detail by Compton (1960), and later by Wyld et al. (2001) and Ciavarella and Wyld (2008). For structural and wall-rock metamorphic relations of the intrusions, the reader is referred to these earlier studies. In this section, we focus on basic field observations and petrography of the six main intrusions named above. A comprehensive suite of samples was collected from each of the six intrusions. Sample locations are reported in Data Repository Table DR1[1]. Modal mineralogy was determined from these samples by point counting of thin sections (1500 points counts per section; Table 1; Fig. 3). The average modal mineralogy for each of the six intrusions is summarized in the following sections.

Granite Peak Stock

The Granite Peak stock is the northernmost intrusion exposed within the SRR. In plan view, it is broadly circular with an approximate diameter of 2.5–3 km (Fig. 2). The stock is texturally heterogeneous, ranging from porphyritic biotite granite with conspicuous orthoclase feldspar megacrysts (1–8 cm) to equigranular biotite granite with large quartz aggregates (~0.5 cm to 1 cm). Predominant minerals are plagioclase (~36%), quartz (~31%), and alkali feldspar (~25%). Minor phases are biotite (~6%) and muscovite (~1%) (Fig. 3; Table 1). Only one sample (RS91-1A) contains trace garnet (<1%). Amphibole and sphene are absent. Garnet and muscovite bearing aplite dikes, quartz and muscovite veins, and lenses of pegmatitic leucogranite are locally common within the stock, especially toward the eastern contact.

Sawtooth Stock

The Sawtooth stock is a prominent leucocratic intrusion exposed along the western side of the SRR, east of the town of Orovada, Nevada. In plan view, the intrusion is roughly circular with a mean diameter of ~2 km (Fig. 2). The stock ranges from biotite granodiorite to equigranular biotite granite. Sawtooth biotite granite-granodiorite is similar in composition to biotite granite of the Granite Peak stock, but contains more plagioclase (~43%), slightly less quartz (~27%) and alkali feldspar (~22%), and lacks garnet and an orthoclase feldspar megacrytic phase (Fig. 3, Table 1). Like the Granite Peak stock, the Sawtooth stock contains trace muscovite and lacks amphibole and sphene (Table 1). The stock is cut by fine-grained aplite dikes containing minor garnet as well as quartz veins similar to those observed within the Granite Peak stock. As noted by Ciavarella and Wyld (2008), the Sawtooth stock also contains a multitude of dikes and apophyses that intrude into the local wall rocks on the northern and southern sides, forming an irregular "sawtooth" contact pattern.

Santa Rosa Pluton

The Santa Rosa pluton occupies the core of the SRR and has an exposed area of ~90 km^2 (Fig. 2). The pluton is generally elongate in a NE-SW direction, broadly paralleling the regional trend of the Triassic stratigraphy and Jurassic wall-rock structures (Compton, 1960; Ciavarella and Wyld, 2008). The predominant rock type within the Santa Rosa pluton is an equigranular hornblende biotite granodiorite with minor quartz monzodiorite and biotite granite (Fig. 3; Table 1). Major phases in the granodiorite and quartz monzodiorite are plagioclase (~48%), quartz (~20%), alkali feldspar (~17%), and biotite (~11%). Most samples contain minor hornblende (~3%) and trace sphene (~1%). Muscovite is absent. Biotite granite contains a similar percent of biotite (~13%), but less plagioclase (~38%), slightly more quartz (~25%) and alkali feldspar (~23%), and lacks hornblende and sphene. Mafic enclaves rich in biotite, hornblende, and plagioclase, with generally circular or ellipsoidal shapes, are locally present, as are schlieren defined by an increase in the modal concentration of biotite (±hornblende).

The Santa Rosa pluton is crosscut by two generations of felsic dikes that appear to be broadly synplutonic (Compton, 1960; Stuck, 1993). These dikes include fine-grained aplite and fine-grained tonalite-granodiorite. Aplite dikes are primarily composed of quartz, alkali-feldspar, and plagioclase (±minor biotite). Tonalite-granodiorite dikes are texturally more complex, ranging from equigranular to porphyritic with phenocrysts of hornblende, plagioclase, and biotite. Both dike sets range from 1 cm to >1 m in thickness.

Andorno Stock

The Andorno stock is exposed in the southwest SRR. In plan view, the stock is broadly circular with a mean diameter of ~2 km (Fig. 2). The stock is predominantly composed of equigranular biotite hornblende granodiorite and granite (Fig. 3; Table 1). Major phases in the granodiorite and granite

[1]GSA Data Repository Item 2018123, which contains complete data tables (Tables DR1–DR7) and additional supporting color figures (Figs. DR1–DR5), is available at http://www.geosociety.org/datarepository/2018, or on request from editing@geosociety.org.

TABLE 1. SAMPLE INFORMATION AND MODAL MINERALOGY OF THE SANTA ROSA RANGE AND BLOODY RUN HILLS GRANITOIDS

Sample information*		Modal mineralogy (vol%)									
Sample number	Rock name	Plagioclase	K-Feldspar	Quartz	Biotite	Muscovite	Amphibole	Sphene	Garnet	Oxides	Accessory†
Granite Peak stock											
KB11-02	Bt. granite	34.5	26.1	31.8	7.0	0.2	0.0	0.0	0.0	0.2	0.2
KB11-03	Bt. granite	28.5	23.3	37.8	7.2	3.0	0.0	0.0	0.0	0.1	0.1
KB11-05	Bt. granite	41.0	23.8	28.3	5.6	0.8	0.0	0.0	0.0	0.3	0.2
KB11-12	Bt. granite	34.6	23.2	34.9	5.3	1.2	0.0	0.0	0.0	0.6	0.2
RS91-1A	Bt. granite	32.5	26.5	34.6	4.2	1.8	0.0	0.0	0.1	0.2	0.1
RS91-4B	Bt. granite	40.1	25.8	24.6	9.3	0.0	0.0	0.0	0.0	0.1	0.1
RS91-8A	Bt. granite	41.8	23.5	28.2	6.1	0.0	0.0	0.0	0.0	0.2	0.2
RS91-10	Bt. granite	36.0	27.0	26.2	10.2	0.0	0.0	0.0	0.0	0.5	0.1
Sawtooth stock											
KB11-14	Bt. granite	40.5	23.0	30.5	5.0	0.6	0.0	0.0	0.0	0.2	0.2
KB11-16	Bt. granite	46.6	21.3	24.5	6.8	0.3	0.0	0.0	0.0	0.3	0.2
RS91-33	Bt. granodiorite	44.5	20.2	25.2	9.5	0.0	0.0	0.0	0.0	0.5	0.1
RS91-37	Bt. granodiorite	43.5	21.5	28.5	3.3	2.5	0.0	0.0	0.0	0.5	0.2
Andorno stock											
KB11-20	Hbl. Bt. granodiorite	47.0	11.5	21.8	12.7	0.0	5.3	1.0	0.0	0.4	0.3
KB11-21	Bt. granite	38.5	22.6	27.2	10.8	0.0	0.0	0.5	0.0	0.2	0.2
KB11-22	Hbl. Bt. granite	43.8	15.6	25.1	11.2	0.0	3.0	0.7	0.0	0.3	0.3
RS91-40B	Hbl. Bt. granodiorite	41.5	20.2	22.5	12.6	0.0	1.5	0.5	0.0	1.0	0.2
RS91-41	Hbl. Bt. granite	40.3	22.5	24.8	9.5	0.0	1.5	0.2	0.0	1.0	0.2
Santa Rosa pluton											
KB11-25	Hbl. Bt. granodiorite	44.5	18.6	24.3	7.8	0.0	3.3	0.8	0.0	0.5	0.2
RS91-19	Bt. granite	38.1	23.2	25.4	12.8	0.0	0.0	0.0	0.0	0.4	0.1
RS91-24A	Quartz monzodiorite	56.3	12.3	13.1	10.0	0.0	6.0	1.0	0.0	1.0	0.3
RS91-28A	Hbl. Bt. granodiorite	51.1	15.3	18.5	9.1	0.0	4.3	1.0	0.0	0.5	0.2
RS91-17A	Hbl. Bt. granodiorite	48.2	16.3	20.0	13.5	0.0	1.2	0.0	0.0	0.5	0.3
RS91-22	Hbl. Bt. granodiorite	45.2	19.6	17.8	15.0	0.0	1.3	0.4	0.0	0.5	0.2
RS91-23	Quartz monzodiorite	46.8	17.5	16.1	17.2	0.0	1.0	0.5	0.0	0.6	0.3
RS91-27B	Quartz monzodiorite	53.5	14.5	16.0	9.6	0.0	4.5	1.2	0.0	0.5	0.2
RS91-30	Hbl. Bt. granodiorite	46.8	14.5	23.0	6.2	0.0	8.0	0.8	0.0	0.5	0.2
RS91-38A	Bt. granodiorite	55.9	12.7	17.9	12.3	0.0	0.0	0.0	0.0	1.0	0.2
RS91-12	Hbl. Bt. granodiorite	49.3	16.8	18.9	12.3	0.0	1.5	0.6	0.0	0.5	0.1
RS91-29A	Hbl. Bt. granodiorite	44.9	20.7	24.1	8.1	0.0	1.0	0.5	0.0	0.5	0.2
RS91-44A	Hbl. Bt. granodiorite	46.5	20.5	21.4	9.4	0.0	1.4	0.0	0.0	0.5	0.3
Bloody Run stock											
RS91-32	Hbl. Bt. granodiorite	46.4	18.5	21.8	8.0	0.0	3.8	0.7	0.0	0.5	0.3
RS91-42	Hbl. Bt. granodiorite	46.3	17.8	21.2	9.8	0.0	3.5	0.8	0.0	0.5	0.1
RS91-43	Hbl. Bt. granodiorite	41.8	21.2	23.1	7.8	0.0	4.7	0.6	0.0	0.5	0.3
Flynn stock											
KB11-09	Hbl. Bt. granodiorite	44.8	18.9	20.4	9.8	0.0	4.2	0.8	0.0	0.8	0.3
KB11-10	Hbl. Bt. granodiorite	45.2	15.2	20.3	9.5	0.0	7.8	1.2	0.0	0.5	0.3
KB11-28	Hbl. Bt. granodiorite	49.8	14.0	19.8	11.0	0.0	4.0	0.8	0.0	0.5	0.1
RS91-31B	Hbl. Bt. granodiorite	45.3	16.2	17.3	17.2	0.0	2.5	0.8	0.0	0.5	0.2

Note: Bt.—biotite; Hbl.—hornblende.
*Table DR1 contains all sample locations (see text footnote 1).
†Accessory phases include zircon, apatite, monazite, and allanite.

are plagioclase (~43%), quartz (~24%), alkali feldspar (~19%), and biotite (~11%). Most samples contain minor hornblende (~2%) and trace sphene (~1%). Muscovite is absent. Like the Santa Rosa pluton, the Andorno stock contains mafic enclaves and is cut by aplitic and tonalite-granodiorite dikes.

Flynn Stock

The Flynn stock is the northernmost stock within the BRH and has an exposed area of ~28 km^2 (Fig. 2). The stock has a broadly elliptical shape in the E-W direction and is located within the hinge of a megascopic Jurassic anticline that extends from the SRR through the BRH (Compton, 1960; Ciavarella and Wyld, 2008). The stock is predominantly composed of hornblende biotite granodiorite (Fig. 3, Table 1). Major phases are plagioclase (~46%), quartz (~20%), alkali feldspar (~16%), and biotite (~12%). Minor phases include hornblende (~5%) and sphene (~1%). Muscovite is absent. The stock also contains fine-grained mafic enclaves and is cut by fine-grained aplite and tonalite-granodiorite dikes.

Bloody Run Stock

The Bloody Run stock is the southernmost intrusion within the BRH and has an exposed area of ~48 km^2 (Fig. 2). It is located within the hinge region of the same megascopic Jurassic anticline as the Flynn stock (Ciavarella and Wyld, 2008). The Bloody Run stock is composed predominantly of hornblende biotite granodiorite. Modal mineralogy of the stock is nearly identical to the Flynn stock (Table 1): plagioclase (~45%), quartz

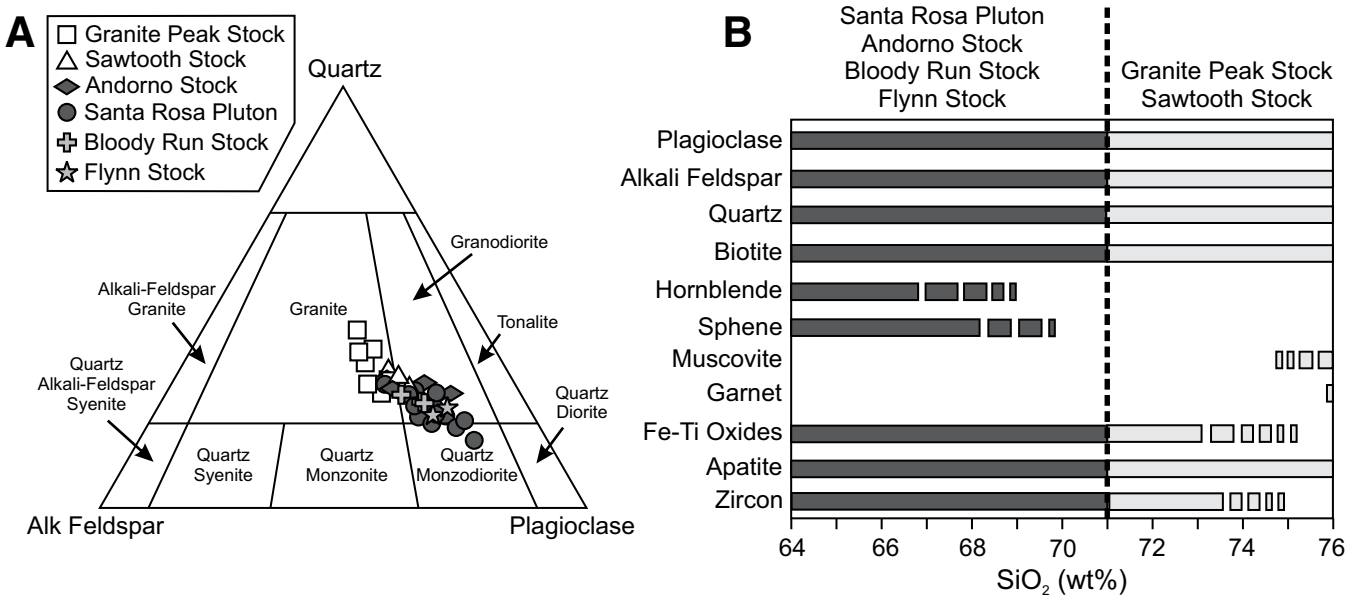

Figure 3. (A) International Union of Geological Sciences classification plot (Streckeisen, 1976) showing the compositional range of Santa Rosa Range and Bloody Run Hills (SRR-BRH) granitoids. Symbols used in this plot are used in all plots. (B) Dominant mineral phases present within the SRR-BRH granitoids relative to whole rock SiO_2 (wt%) (after Stuck, 1993). Solid lines indicate that the mineral is present in all examined samples at that wt% SiO_2. Dashed lines indicate that the mineral is present in some of the samples at that wt% SiO_2. No line indicates that the mineral was not observed within any of the samples at that wt% SiO_2. The modal mineralogy is reported in Table 1.

(~22%), alkali feldspar (~19%), biotite (~9%), hornblende (~4%), and sphene (~1%). Although no enclaves or crosscutting dikes were observed as part of this study, Ciavarella and Wyld (2008) indicate that the Bloody Run stock contains quartz dioritic enclaves and granodiorite dikes.

Synthesis of Field Observations and Petrography

Field and petrographic observations indicate the presence of two distinct granitoid groups within the SRR-BRH. The Granite Peak and Sawtooth stocks are characterized as biotite granite-granodiorite intrusions with minor mafic phases (only biotite, no hornblende or sphene), and contain trace muscovite and rare garnet. The Santa Rosa pluton, Andorno stock, Flynn stock, and Bloody Run stock are primarily hornblende biotite granodiorite intrusions that are characterized by a greater proportion of mafic phases (biotite and hornblende), contain sphene, and lack muscovite and garnet (Fig. 3; Table 1). Other important distinctions between the two granitoid groups are the presence of mafic enclaves, schlieren, and crosscutting dike compositions. The Granite Peak and Sawtooth stocks lack mafic enclaves and schlieren and are cut by garnet-bearing aplite dikes. The hornblende biotite granodiorite intrusions contain mafic enclaves and schlieren, and are cut by aplite (no observed garnet) and more mafic tonalite-granodiorite dikes.

Based on field and petrographic observations, we define the two granitoid groups as: (1) the Santa Rosa/Andorno (SRA) group, which includes the Santa Rosa pluton, Andorno stock, Flynn stock, and Bloody Run stock; and (2) the Granite Peak/Sawtooth (GPS) group that includes the Granite Peak and the Sawtooth stocks. Stuck (1993) originally defined these two groups (SRA and GPS) in the SRR. Because the BRH intrusions (Flynn and Bloody Run stocks) immediately to the south share many similarities to the SRA group in the SRR, we include the BRH intrusions in the SRA group. Age, chemical, and isotopic data presented in the following sections further support this twofold subdivision.

U-Pb ZIRCON GEOCHRONOLOGY

Eleven samples from the six SRR-BRH intrusions were selected for laser-ablation multi-collector inductively coupled plasma–mass spectrometry (LA-MC-ICP-MS) U-Pb zircon geochronology. These include three samples from the Santa Rosa pluton, two samples from the Granite Peak, Sawtooth, and Andorno stocks, and one sample from the Flynn and Bloody Run stocks. Methods of zircon separation and analysis are presented in the Data Repository Item. New U-Pb zircon analytical results presented in this study are reported at 2σ uncertainty and are detailed in Data Repository Figures DR2a, DR2b, and DR2c, Table DR2, and summarized in Figure 4.

The results for each intrusion are presented separately, and within this discussion, the terminology of Miller et al. (2007) is used to help distinguish among (1) xenocrystic zircons—zircons that are clearly inherited from the host-rock or source, and (2) autocrystic zircons—zircons that are interpreted to have crystallized from the intrusion in which they reside. Only autocrystic rim analyses were used in the weighted mean age calculations. While we recognize that magmatic systems such as these may be constructed incrementally with punctuated periods of melt replenishment and zircon growth, the 2σ uncertainty of the U-Pb zircon method used in this study limits the ability to resolve the timing of short-lived events/processes operating within these intrusions (i.e., events <1.0 Ma). Thus, we do not use the term, antecryst, which is defined as a zircon that crystallized from an earlier pulse of magma that becomes incorporated into a later pulse (e.g., Miller et al., 2007). However, it is important to note that the consistency of concordant autocrystic rim ages (within 2σ uncertainty) reported for each intrusion suggests that the weighted mean U-Pb ages encompass the timing of potential short-lived magmatic events/processes operating in these intrusions, and therefore, the final reported age likely reflects the average crystallization age for each intrusion. In subsequent discussions this simply is referred to as the crystallization age of a given intrusion.

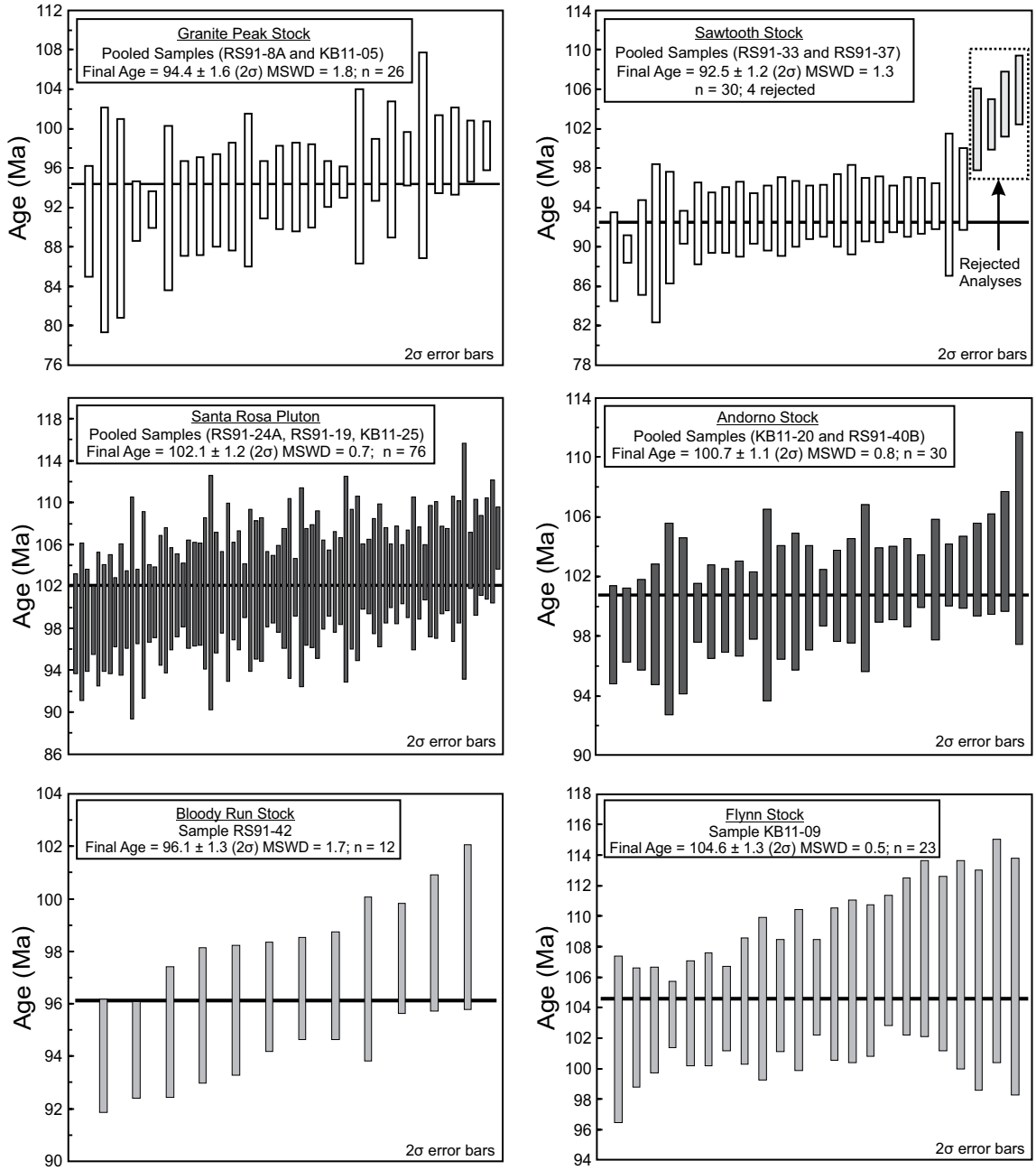

Figure 4. Weighted mean zircon U-Pb age plots for the Santa Rosa Range and Bloody Run Hills (SRR-BRH) granitoids showing pooled U-Pb zircon analyses used to determine crystallization ages for each intrusion. Pooled samples are listed for each intrusion. Individual U-Pb ages are reported in Table DR2. Final ages include both the analytical uncertainty and a systematic uncertainty, quoted at the 2σ level (see Gehrels et al., 2008). Error bars are shown at the 2σ level. Interpreted crystallization ages, including 2σ uncertainties, were generated using routines in Isoplot (Ludwig, 2008).

Granite Peak Stock

No prior isotopic ages have been obtained from the Granite Peak stock, which is shown as of uncertain Jurassic-Tertiary age in the compilation of du Bray (2007). Two biotite granite samples from this stock were selected for U-Pb zircon analysis (KB11-05 and RS91-8A). Both samples yield abundant prismatic, euhedral zircons (Fig. DR1a). A majority of the zircons (~82%) from both samples are interpreted as autocrystic, as their cores and rims yield a consistent U-Pb age within 2σ uncertainty and have continuous to nearly continuous core to rim oscillatory zoning. Cathodoluminescence (CL)-imaging and U-Pb analyses indicate that ~18% of the zircons have xenocrystic cores. These xenocrystic cores have much older U-Pb ages that range from ca. 164 to ca. 1665 Ma (Table DR2), and are identified by rounded and embayed core regions overgrown by rims with well-developed zoning. Autocrystic zircon rims from the two Granite Peak samples yield the following weighted mean ages (reported at 2σ uncertainty): KB11-05 = 93.7 ± 2.1 Ma; RS91-8A = 95.1 ± 1.5 Ma (Fig. DR2a). Individual autocrystic rim ages were pooled from both biotite granite samples and yield a final weighted mean age of 94.4 ± 1.6 Ma (2σ; n = 26; MSWD = 1.8) (Fig. 4). This pooled weighted mean age is the interpreted crystallization age of the Granite Peak stock.

Sawtooth Stock

No prior isotopic ages have been obtained from the Sawtooth stock, which is shown as of uncertain Jurassic-Tertiary age in the compilation of du Bray (2007). Two biotite granodiorite samples from the Sawtooth stock were selected for U-Pb zircon analysis (RS91-37 and RS91-33). Both samples contain abundant (~74%) euhedral, autocrystic zircons that display continuous to nearly-continuous core to rim oscillatory zoning and yield U-Pb ages that overlap within 2σ uncertainty. Approximately 26% of the zircons have embayed and rounded xenocrystic core regions that yield much older U-Pb ages (ca. 129 to ca. 1395 Ma) (Table DR2). Autocrystic zircon rims from the two samples yield the following weighted mean ages (reported at 2σ uncertainty): RS91-37 = 91.3 ± 1.7 Ma; RS91-33 = 93.6 ± 1.4 Ma (Fig. DR2a). Individual autocrystic zircon rims were pooled from both samples and yield a final weighted mean age of 92.5 ± 1.2 Ma (2σ; n = 26 of 30; 4 rejected; MSWD = 1.3) (Fig. 4). This age is the interpreted crystallization age of the Sawtooth stock.

Santa Rosa Pluton

Several prior studies have obtained isotopic age data for the Santa Rosa pluton. These include K/Ar hornblende/biotite (99.5 ± 5.0 Ma/97.8 ± 3.5 Ma, Smith et al., 1971; 102.0 ± 5.0 Ma/100.2 ± 3.5 Ma, Elison et al., 1990) and U-Pb zircon ages (105.1 ± 1.1 Ma, Colgan et al., 2006). We have complemented the existing database with U-Pb zircon analyses from three new Santa Rosa pluton samples (RS91-24A, KB11-25, RS91-19) that span the full compositional range of the intrusion (~64, ~69, and ~71 wt% SiO_2, respectively). All three samples contain abundant euhedral, autocrystic zircons (~88%) that contain well-developed core to rim oscillatory zoning and yield U-Pb ages within 2σ uncertainty. Approximately 12% of the zircon grains from all three samples contain rounded and embayed xenocrystic core regions surrounded by well-developed oscillatory zoned rims. U-Pb ages for these xenocrystic cores range from ca. 188–1974 Ma (Table DR2). Autocrystic zircons from the three samples yield the following weighted mean ages (reported at 2σ uncertainty): RS91-24A = 101.3 ± 1.3 Ma; KB11-25 = 102.8 ± 1.3 Ma; RS91-19 = 102.1 ± 1.5 Ma (Figs. DR1b, DR2b, and DR2c). Pooling individual autocrystic zircon rim ages from all three samples produces a final weighted mean age of 102.1 ± 1.2 Ma (2σ; n = 76; MSWD = 0.7) (Fig. 4). This age is the interpreted crystallization age of the Santa Rosa pluton, and is in good agreement with prior isotopic ages obtained for the pluton.

Andorno Stock

The only prior isotopic age analysis of the Andorno stock is a U-Pb zircon age of 102.4 ± 1.0 Ma presented by Wyld et al. (2001). We obtained two additional hornblende biotite granodiorite samples from the Andorno stock for U-Pb analyses (KB11-20 and RS91-40B). A majority of the zircons (~65%) in both samples are interpreted as autocrystic, as their cores and rims yield the same age within 2σ uncertainty and have continuous core to rim oscillatory zoning. CL-imaging and U-Pb age analyses indicate that approximately ~35% of the zircons are xenocrystic, containing rounded and embayed core regions with much older U-Pb ages (e.g., ca. 250 to ca. 2164 Ma; Fig. DR1b and Table DR2). Autocrystic zircons from the two samples yield the following weighted mean U-Pb ages (reported at 2σ uncertainty): RS91-40B = 100.3 ± 1.3 Ma; KB11-20 = 100.7 ± 1.2 Ma (Figs. DR1b and DR2b). Individual autocrystic rims were pooled from both samples and yield a final weighted mean age of 100.7 ± 1.1 Ma (2σ; n = 30; MSWD = 0.8) (Fig. 4). This is the interpreted crystallization age of the Andorno stock, and is in close agreement with the U-Pb zircon age obtained by Wyld et al. (2001).

Flynn Stock

No prior isotopic ages have been obtained from the Flynn stock, which is shown simply as of uncertain Jurassic-Tertiary age in the compilation of du Bray (2007). Due to its limited compositional variability (hornblende biotite granodiorite), only one sample was selected from the Flynn stock (KB11-09). With the exception of one grain, all of the zircons from this sample are autocrystic, revealing continuous core to rim oscillatory zoning and yielding a consistent U-Pb age within 2σ uncertainty. The one exception contains a xenocrystic zircon core that yields an age of ca. 1124 Ma. The autocrystic zircon rims yield a weighted mean U-Pb age of 104.6 ± 1.3 Ma (2σ; n = 23; MSWD = 0.5) (Fig. 4; Figs. DR1c and DR2c). This is the interpreted crystallization age of the Flynn stock.

Bloody Run Stock

The only prior isotopic age analysis of the Bloody Run stock is a U-Pb zircon age of 97.7 ± 0.7 Ma presented in Colgan et al. (2006). We obtained one additional hornblende biotite granodiorite sample (RS91-42) for U-Pb zircon analyses. Similar to the Flynn stock, all of the zircons except one grain are interpreted as autocrystic. These autocrystic zircons reveal continuous core to rim oscillatory zoning and yield a consistent U-Pb age within 2σ uncertainty. The one exception contains a xenocrystic zircon core that yields an age of ca. 269 Ma (Table DR2). Using only autocrystic rim analyses, this sample produced a weighted mean U-Pb age of 96.1 ± 1.3 Ma (2σ; n = 12; MSWD = 1.7) (Fig. 4; Figs. DR1c and DR2c). This is the interpreted crystallization age of the Bloody Run stock, and is in close agreement with the U-Pb age obtained by Colgan et al. (2006).

Synthesis of U-Pb Zircon Geochronology

New U-Pb zircon ages for the six SRR-BRH intrusions are summarized as follows (reported at 2σ uncertainty): Granite Peak stock (94.4 ± 1.6 Ma); Sawtooth stock (92.5 ± 1.2 Ma); Santa Rosa pluton (102.1 ± 1.2 Ma); Andorno stock (100.7 ± 1.1 Ma); Flynn stock (104.6 ± 1.3 Ma); and Bloody Run stock (96.1 ± 1.3 Ma) (Fig. 4). These new ages complement and expand the available SRR-BRH granitoid chronology, and where

overlap exists, the new ages are in good agreement with existing information (K/Ar hornblende/biotite, Smith et al., 1971; Elison et al., 1990; and U-Pb zircon ages, Wyld et al., 2001; Colgan et al., 2006).

Both new and prior isotopic age data support the presence of two distinct granitoid groups within the SRR-BRH. The older suite is defined by the SRA group (Santa Rosa pluton, 105–102 Ma; Andorno stock, 102–100 Ma; Flynn stock, 104 Ma; Bloody Run stock, 98–96 Ma), while the younger suite is defined by the GPS group (Granite Peak stock, 94 Ma; Sawtooth stock, 92.5 Ma) (Fig. 4). Xenocrystic zircon cores are also present in all of the SRR-BRH intrusions, and include early Mesozoic, Paleozoic, and Proterozoic ages (Table DR2).

INTRUSION THERMOMETRY AND BAROMETRY

Using hornblende and plagioclase mineral compositions, estimated solidus pressures and temperatures were determined for selected granodiorite samples from the Santa Rosa pluton, Flynn stock, and Bloody Run stock (SRA group granitoids). The other stocks were not analyzed because they lacked hornblende or did not contain a mineral assemblage appropriate for the Al-in-hornblende thermobarometer, as outlined by Anderson (1996) and Anderson et al. (2008). Al-in-hornblende analytical methods are detailed in the Data Repository Item.

Estimated solidus pressures and temperatures were simultaneously solved using the plagioclase–amphibole thermometer (reaction B) of Holland and Blundy (1994) and the temperature dependent Al-in-hornblende barometer of Anderson and Smith (1995). Plagioclase and hornblende compositions used in these calculations are presented in Table 2. Individual plagioclase compositions reported in Table DR4 correspond to spot numbers shown in Table 2. Estimated solidus pressures and temperatures for the intrusions (Santa Rosa pluton, Flynn stock, and Bloody Run stock) are reported in Table 2 and illustrated in Figure DR3.

The Santa Rosa pluton (n = 6 hornblende and plagioclase pairs) yielded an average estimated solidus temperature and pressure of 712 ± 14 °C and 0.13 ± 0.05 GPa. The Flynn stock produced a nearly identical average temperature and pressure (n = 6 pairs; 710 ± 16 °C and 0.12 ± 0.04 GPa). The Bloody Run stock, however, yielded a similar temperature (716 ± 26 °C) but a higher average pressure (0.28 ± 0.04 GPa). Because these temperature and pressure estimates are at or slightly above the granite and tonalite solidii (Fig. DR3; solidii from Anderson et al., 2008), they are interpreted to represent the final emplacement conditions for these intrusions.

Synthesis of Thermometry and Barometry

Using an average crustal density of ~2.7 g/cm^3, these new pressure estimates correspond to emplacement depths of ~5–10 km. Field observations such as andalusite-bearing contact aureoles (Compton, 1960; Barton et al., 1988; Maffei, 1992; Rogers, 1999; Ciavarella and Wyld, 2008), low-temperature microstructures (bulging recrystallization in quartz ≤300 °C, Purcell et al., 2012), slaty cleavage development (Amato, 1998), and relict sedimentary structures (ripples and cross bedding; Rogers, 1999; Wyld et al., 2001; Purcell et al., 2012) preserved within the Triassic metasedimentary wall-rocks are consistent with these shallow crustal depths. Based on the presence of andalusite-bearing contact aureoles and the absence of caldera remnants and other shallow volcanic features, Colgan et al. (2006) argued that the SRR-BRH intrusions were emplaced at depths of ~3–11 km. Similarly, Ciavarella and Wyld (2008) estimated emplacement depths of 7–12 km for the SRR-BRH intrusions. The new Al-in-hornblende thermobarometry results presented in this study are in good agreement with these prior depth estimates and indicate that the SRA group intrusions represent shallow crustal magmatic systems.

Emplacement depths have previously been estimated for the GPS group intrusions. Colgan et al. (2006) argued that the depth of exposure of the Mesozoic crustal column varies by ~4 km from the southeast to the northwest in the SRR. Thus, intrusions exposed in the northwest SRR are slightly deeper than intrusions in the southeast. Ciavarella and Wyld (2008) inferred the emplacement depths for the Granite Peak and Sawtooth stocks based on contact metamorphic mineral assemblages, wall-rock structural relationships, and emplacement mechanisms. Contact metamorphic mineral assemblages around the Sawtooth stock indicate emplacement depths of ~10.5–12 km (Maffei, 1992; Rogers, 1999; Ciavarella and Wyld, 2008). Similar mineral assemblages are observed in the contact aureoles surrounding the Granite Peak stock, suggesting a comparable emplacement depth (Ciavarella and Wyld, 2008). Collectively, these observations suggest slightly deeper emplacement depths for the GPS group granitoids (~10.5–12 km), and agree with the presence of primary muscovite in these intrusions (e.g., Miller and Bradfish, 1980).

BULK ROCK MAJOR AND TRACE ELEMENT GEOCHEMISTRY

A representative suite of major and trace element analyses is provided in Table 3. All analyses are reported in Table DR5 and are displayed in Figs. 5–7. Bulk major and trace element analytical methods are detailed in the Data Repository Item.

All of the granitoid intrusions have calc-alkaline compositions characteristic of granitoids emplaced in continental arc settings worldwide (Figs. 5A and 5B). With the exception of two Bloody Run stock samples (~66 wt% SiO_2), all of the SRR-BRH granitoids plot within the "calc-alkalic" field of Frost et al. (2001). Additionally, all of the samples fall within the "volcanic arc granite" field of Pearce et al. (1984) (Figs. 5A and 5B).

Bulk chemical variation diagrams provide strong support for the two distinct groups established earlier (SRA and GPS groups). A plot of aluminum saturation index (A/CNK, after Shand, 1969) versus SiO_2 highlights the presence of these two groups (Fig. 5C). The SRA granitoids form a low-silica group dominated by metaluminous to weakly peraluminous compositions. The GPS granitoids form a high-silica group restricted to peraluminous compositions. Similarly, a plot of Fe* (Fe* = FeO_{tot}/(FeO_{tot} + MgO) after Frost et al. 2001) versus SiO_2 clearly defines the two chemical groupings (Fig. 5D). Both groups are classified as "magnesian" (calc-alkaline: Miyashiro, 1974) with the SRA group being characterized by lower silica and lower Fe* than the GPS group. These two chemical groups are clear in all major and trace element geochemical plots (Figs. 5–7).

With the exception of Na_2O and K_2O, all of the major element oxides decrease systematically with increasing silica (Fig. 6). However, in most cases, a break or inflection in the major element trends occurs at ~71–72 wt% SiO_2, coincident with the transition from the SRA to the GPS granitoids. These observed inflections are clear in the TiO_2, Al_2O_3, CaO, Fe_2O_3*, and MgO plots (~71–72 wt% SiO_2) (Fig. 6). In general, the SRA group has lower SiO_2 and K_2O, higher TiO_2, Al_2O_3, MnO, MgO, Fe_2O_3*, P_2O_5, and similar Na_2O concentrations compared to the GPS group (Fig. 6).

The presence of two distinct chemical groups is further emphasized when trace elements of differing behavior are plotted versus silica (Fig. 7). Strontium (Sr) shows a decrease with increasing silica in both the SRA and GPS groups. The least evolved GPS sample is nearly 150 ppm higher in Sr than the most evolved SRA sample at the same silica content (~71–72 wt% SiO_2) (Fig. 7). This relationship yields two sub-parallel trends of decreasing Sr with increasing silica. A similar situation is observed for the element Th (Fig. 7). These sub-parallel trends clearly distinguish the intrusions that define the SRA and GPS groups.

The two groups manifest differently in other LILE plots. For example, there is a nearly continuous trend from the low-Rb SRA granitoids to the

TABLE 2. HORNBLENDE AND PLAGIOCLASE PAIR COMPOSITIONS FOR AI-HORNBLENDE THERMOBAROMETRY

	Santa Rosa pluton						Bloody Run stock			Flynn stock					
Sample:	RS91-24A	RS91-24A	RS91-24A	RS91-24A	RS91-24A	KB11-25	RS91-42	RS91-42	RS91-42	KB11-09	KB11-09	KB11-09	KB11-28	KB11-28	KB11-28
Hornblende*:	#67	#70	#71	#72	#76	#234	#220	#221	#228	#152	#156	#159	#168	#169	#179
Location:	Rim	Rim	Rim	Rim	Rim	Rim	Rim	Rim	Rim	Rim	Rim	Rim	Rim	Rim	Rim
Major elements (wt%)															
SiO_2	49.23	49.43	49.04	49.48	49.01	47.67	47.12	45.90	46.08	49.72	49.15	49.42	49.23	50.03	48.11
TiO_2	0.75	0.78	0.81	0.77	0.80	1.18	1.09	1.10	1.11	0.78	0.80	0.84	0.82	0.73	0.90
Al_2O_3	5.55	5.33	5.80	5.25	5.76	6.16	7.18	7.79	7.91	5.44	5.79	5.58	5.50	5.13	5.77
$FeO_{(tot)}$	15.30	14.57	15.23	14.88	15.73	15.86	15.74	16.37	16.31	14.42	14.32	14.14	14.85	14.59	15.24
MgO	14.14	14.14	13.56	14.20	13.62	12.96	12.81	12.12	12.31	14.17	14.06	14.35	13.93	14.30	13.28
MnO	0.58	0.56	0.69	0.59	0.71	0.87	0.71	0.66	0.71	0.49	0.60	0.57	0.49	0.49	0.56
CaO	11.67	11.37	11.58	11.57	11.61	11.49	11.50	11.64	11.70	11.89	11.70	11.87	11.67	11.93	11.82
NaO	0.90	0.96	0.92	0.84	1.02	1.07	1.05	1.16	1.13	0.85	0.86	0.81	0.92	0.82	0.97
K_2O	0.30	0.41	0.34	0.37	0.34	0.57	0.53	0.70	0.65	0.41	0.34	0.44	0.38	0.38	0.45
H_2O	2.05	2.04	2.04	2.05	2.05	2.02	2.02	2.00	2.01	2.06	2.04	2.03	2.04	2.06	2.02
Total	100.48	99.60	100.00	100.01	100.65	99.84	99.75	99.44	99.92	100.23	99.66	100.05	99.84	100.45	99.12
Cations															
Si	7.20	7.26	7.20	7.25	7.17	7.07	6.99	6.87	6.86	7.25	7.21	7.22	7.23	7.28	7.15
Ti	0.08	0.09	0.09	0.09	0.09	0.13	0.12	0.12	0.12	0.09	0.09	0.09	0.09	0.08	0.10
Al	0.96	0.92	1.00	0.91	0.99	1.08	1.25	1.38	1.39	0.94	1.00	0.96	0.95	0.88	1.01
Fe	1.87	1.79	1.87	1.82	1.93	1.97	1.95	2.05	2.03	1.76	1.76	1.73	1.82	1.78	1.90
Mg	3.08	3.10	2.97	3.10	2.97	2.87	2.83	2.71	2.73	3.08	3.08	3.12	3.05	3.10	2.94
Mn	0.07	0.07	0.09	0.07	0.09	0.11	0.09	0.08	0.09	0.06	0.08	0.07	0.06	0.06	0.07
Ca	1.83	1.79	1.82	1.82	1.82	1.83	1.83	1.87	1.87	1.86	1.84	1.86	1.84	1.86	1.88
Na	0.26	0.27	0.26	0.24	0.29	0.31	0.30	0.34	0.33	0.24	0.25	0.23	0.26	0.23	0.28
K	0.06	0.08	0.06	0.07	0.06	0.11	0.10	0.13	0.12	0.08	0.06	0.08	0.07	0.07	0.09
Total	15.40	15.37	15.37	15.37	15.42	15.47	15.47	15.47	15.47	15.35	15.35	15.36	15.37	15.35	15.42
Fe/(Fe+Mg)	0.38	0.37	0.39	0.37	0.39	0.41	0.41	0.43	0.43	0.36	0.36	0.36	0.37	0.36	0.39
Plagioclase†:	#15	#21	#13	#31	#16	#205	#181	#194	#187	#100	#103	#108	#123	#137	#136
Location:	Rim	Rim	Rim	Rim	Rim	Rim	Rim	Rim	Rim	Rim	Rim	Rim	Rim	Rim	Rim
Ab:	0.66	0.63	0.62	0.67	0.69	0.68	0.73	0.72	0.70	0.62	0.63	0.63	0.67	0.63	0.65
An:	0.32	0.35	0.37	0.31	0.30	0.31	0.25	0.27	0.29	0.36	0.36	0.36	0.31	0.35	0.34
Temperature (°C)	705.6	715.0	717.5	702.7	709.7	719.6	702.2	717.0	727.6	705.8	703.9	708.7	701.0	705.3	723.7
Pressue (Kb)	1.2	1.0	1.3	1.1	1.4	1.6	2.6	3.0	2.9	1.2	1.5	1.2	1.3	0.9	1.3

*Table DR3 contains individual hornblende analyses (see text footnote 1).
†Table DR4 contains individual plagioclase analyses (see text footnote 1). Ab—Albite; An—Anorthite.

TABLE 3. REPRESENTATIVE MAJOR AND TRACE ELEMENT ANALYSES OF THE SANTA ROSA RANGE AND BLOODY RUN HILLS GRANITOIDS

Sample:	KB11-02	KB11-05	RS91-8A	RS91-10	CH-7	KB11-16	KB11-17	KB11-18	RS91-33	RS91-37
Rock name:	Bt. granite	Bt. granite	Bt. granite	Bt. granite	Bt. granite	Bt. granite	Bt. granite	Bt. granite	Bt. granodiorite	Bt. granodiorite
Intrusion:	Granite Peak	Granite Peak	Granite Peak	Granite Peak	Granite Peak	Sawtooth	Sawtooth	Sawtooth	Sawtooth	Sawtooth
Major elements* (wt%)										
SiO_2	73.21	72.39	73.37	72.24	73.71	70.51	71.81	72.02	71.06	72.60
TiO_2	0.21	0.23	0.19	0.21	0.20	0.26	0.23	0.22	0.25	0.20
Al_2O_3	15.31	15.59	15.17	15.12	14.97	16.03	15.58	15.50	15.92	15.37
Fe_2O_3 (t)	1.36	1.41	1.29	1.47	1.10	1.74	1.49	1.48	1.63	1.40
MnO	0.03	0.03	0.03	0.04	0.02	0.04	0.04	0.04	0.04	0.04
MgO	0.35	0.34	0.30	0.33	0.13	0.42	0.37	0.35	0.42	0.34
CaO	1.93	2.00	1.82	1.86	1.54	2.37	2.22	2.15	2.31	1.89
Na_2O	4.35	4.43	4.28	3.93	3.87	4.71	4.58	4.55	4.68	4.46
K_2O	3.34	3.13	3.10	3.85	3.42	3.02	2.99	3.07	3.00	3.35
P_2O_5	0.07	0.07	0.07	0.09	0.04	0.07	0.08	0.06	0.08	0.06
LOI	0.45	0.57	0.61	0.49	0.22	0.56	0.46	0.54	0.58	0.58
Total	100.61	100.19	100.23	99.63	99.22	99.73	99.85	99.98	99.97	100.29
A/CNK	1.07	1.09	1.11	1.08	1.16	1.05	1.05	1.05	1.05	1.07
T_{Zr} (°C)	802.8	787.2	792.6	808.7	813.2	774.3	776.0	775.1	785.3	787.1
Trace elements† (ppm)										
Ni	3.0	3.0	4.0	1.0	N.D.§	3.0	3.0	3.0	4.0	4.0
Cr	1.8	1.9	3.7	1.6	4.1	3.1	2.6	2.3	4.1	3.4
Sc	3.0	3.0	4.0	2.0	2.0	3.0	3.0	3.0	5.0	4.0
V	10.8	14.2	13.6	11.0	12.3	23.6	16.5	15.8	23.7	15.4
Ba	1616	1240	1156	1469	1325	1491	1537	1484	1380	1563
Rb	96	106	136	140	132	94	90	85	87	110
Sr	481	460	477	521	521	554	524	509	605	536
Zr	133	111	115	141	136	103	102	100	115	112
Y	8.3	9.3	8.6	7.1	7.8	7.3	8.7	8.4	6.4	7.6
Nb	8.7	9.7	7.5	6.9	8.0	7.3	8.0	7.5	3.9	5.0
Ga	19.4	20.3	19.9	22.2	20.4	19.7	19.3	19.5	18.9	19.4
Cu	1.1	17.0	10.9	8.7	10.2	2.6	1.6	1.2	4.7	1.8
Co	1.2	1.3	1.2	1.2	1.1	1.9	1.5	1.4	1.8	1.4
Zn	37.3	66.1	51.5	75.2	48.4	31.0	23.7	23.4	51.0	50.4
Pb	22.8	19.8	21.5	22.2	24.0	20.0	20.1	20.1	18.5	21.6
U	1.4	1.6	1.6	1.9	4.6	1.0	0.7	0.7	1.2	1.6
Th	10.8	9.2	8.4	9.1	10.8	6.4	8.5	8.3	6.4	7.6
Cs	1.3	2.6	7.3	3.5	3.1	2.3	1.9	1.7	2.4	1.6
Hf	3.7	3.4	3.0	3.1	3.4	3.0	3.0	2.9	2.9	3.0
Ta	0.4	0.7	0.7	0.6	0.6	0.3	0.4	0.4	0.2	0.4
La	25.8	20.8	19.0	26.9	26.4	16.2	23.4	21.3	18.4	21.3
Ce	45.4	38.7	34.6	47.7	47.8	31.1	42.9	39.7	34.2	39.6
Yb	0.54	0.60	0.70	0.43	0.62	0.55	0.50	0.52	0.62	0.66

Sample:	KB11-20	KB11-21	KB11-22	RS91-40B	RS91-41	KB11-25	RS91-19	RS91-24A	RS91-28A	RS91-23
Rock name:	Hbl. bt. granodiorite	Bt. granite	Hbl. bt. granite	Hbl. bt. granodiorite	Hbl. bt. granite	Hbl. bt. granodiorite	Bt. granite	Quartz monzodiorite	Hbl. bt. granodiorite	Quartz monzodiorite
Intrusion:	Andorno	Andorno	Andorno	Andorno	Andorno	Santa Rosa	Santa Rosa	Santa Rosa	Santa Rosa	Santa Rosa
Major elements*(wt%)										
SiO_2	64.82	70.29	66.48	67.26	68.00	69.37	71.08	64.27	68.54	67.64
TiO_2	0.58	0.32	0.48	0.44	0.44	0.36	0.26	0.59	0.41	0.43
Al_2O_3	17.33	15.79	17.02	16.43	16.55	15.95	15.61	17.24	16.24	16.76
Fe_2O_3 (t)	4.01	2.30	3.60	3.10	3.10	2.42	1.66	3.96	2.82	2.67
MnO	0.09	0.06	0.08	0.07	0.07	0.06	0.04	0.08	0.06	0.06
MgO	1.55	0.77	1.21	1.26	1.19	1.22	0.75	2.19	1.38	1.41
CaO	4.17	2.47	3.92	3.06	3.04	2.90	2.01	4.23	3.19	3.33
Na_2O	4.85	4.37	4.74	4.37	4.40	4.73	4.42	4.70	4.88	4.86
K_2O	2.30	3.20	2.47	2.91	2.95	2.72	3.69	1.93	2.41	2.33
P_2O_5	0.22	0.12	0.19	0.18	0.17	0.14	0.10	0.22	0.17	0.17
LOI	0.65	0.39	0.45	0.65	0.48	0.46	0.54	0.56	0.49	0.60
Total	100.57	100.08	100.64	99.73	100.39	100.33	100.16	99.97	100.59	100.26
A/CNK	0.96	1.04	0.97	1.03	1.04	1.00	1.05	0.98	0.99	1.01
T_{Zr} (°C)	787.2	774.7	784.3	799.0	807.6	755.7	791.8	792.7	795.3	808.2
Trace elements† (ppm)										
Ni	6.0	4.0	6.0	6.0	3.0	7.0	5.0	13.0	11.0	7.0
Cr	7.1	4.0	4.6	8.0	6.1	9.7	6.6	20.2	12.8	12.6
Sc	10.0	6.0	8.0	7.0	8.0	6.0	4.0	11.0	8.0	7.0
V	76.9	37.7	62.3	65.8	60.5	51.1	34.7	97.9	62.3	60.0
Ba	1260	1601	1422	1487	1467	1226	1973	1118	1190	1229
Rb	67	101	64	80	81	60	112	52	64	54

(*continued*)

TABLE 3. REPRESENTATIVE MAJOR AND TRACE ELEMENT ANALYSES OF THE SANTA ROSA RANGE AND BLOODY RUN HILLS GRANITOIDS (*continued*)

Sample:	KB11-20	KB11-21	KB11-22	RS91-40B	RS91-41	KB11-25	RS91-19	RS91-24A	RS91-28A	RS91-23
Rock name:	Hbl. bt. granodiorite	Bt. granite	Hbl. bt. granite	Hbl. bt. granodiorite	Hbl. bt. granite	Hbl. bt. granodiorite	Bt. granite	Quartz monzodiorite	Hbl. bt. granodiorite	Quartz monzodiorite
Intrusion:	Andorno	Andorno	Andorno	Andorno	Andorno	Santa Rosa	Santa Rosa	Santa Rosa	Santa Rosa	Santa Rosa
Trace elements† (ppm)										
Sr	579	423	579	560	534	436	409	619	522	553
Zr	158	105	146	151	165	91	122	167	151	173
Y	16.3	8.8	13.9	9.4	11.6	9.7	6.3	13.9	10.8	15.5
Nb	10.8	9.1	9.9	5.4	6.0	8.1	4.2	6.0	7.8	6.8
Ga	20.8	18.9	19.9	19.1	20.2	18.8	17.8	19.3	19.3	20.3
Cu	3.8	2.6	10.1	8.1	18.0	8.0	6.9	22.5	9.6	18.3
Co	6.7	3.4	5.2	5.7	5.5	5.1	3.4	9.4	6.0	5.9
Zn	49.3	26.6	41.2	62.1	74.8	24.2	38.9	64.1	49.7	60.5
Pb	18.5	26.4	17.5	19.8	19.7	21.1	26.7	13.3	18.3	16.3
U	1.3	2.9	2.9	2.7	3.0	1.7	2.5	1.7	1.9	2.6
Th	7.1	9.9	8.4	11.0	8.6	10.5	10.9	7.8	9.9	12.3
Cs	2.5	2.9	2.1	1.6	2.5	1.5	1.7	0.8	1.0	0.9
Hf	4.1	3.1	3.9	3.7	3.6	2.8	3.0	3.9	4.0	3.7
Ta	0.5	0.6	0.6	0.3	0.6	0.6	0.3	0.4	0.6	0.7
La	22.4	20.5	23.4	21.6	20.6	17.7	25.2	23.6	18.6	27.3
Ce	44.1	38.8	45.9	40.3	38.9	34.6	44.2	46.5	37.2	52.4
Yb	1.21	0.76	1.18	0.88	0.89	0.93	0.54	1.29	1.00	1.20

Sample:	RS91-27B	RS91-30	RS91-38A	KB11-09	KB11-10	KB11-28	RS91-31B	RS91-32	RS91-42	RS91-43
Rock name:	Quartz monzodiorite	Hbl. bt. granodiorite	Bt. granodiorite	Hbl. bt. granodiorite	Hbl. bt. granodiorite	Hbl. bt. granodiorite	Hbl. bt. granodiorite	Hbl. bt. granodiorite	Hbl. bt. granodiorite	Hbl. bt. granodiorite
Intrusion:	Santa Rosa	Santa Rosa	Santa Rosa	Flynn	Flynn	Flynn	Flynn	Bloody Run	Bloody Run	Bloody Run
Major elements* (wt%)										
SiO_2	65.85	66.74	66.75	65.10	65.34	66.25	65.94	64.94	65.07	67.95
TiO_2	0.51	0.47	0.49	0.55	0.57	0.58	0.56	0.47	0.45	0.38
Al_2O_3	17.10	16.41	16.44	16.66	16.64	16.15	16.44	16.77	16.83	16.10
Fe_2O_3(t)	3.52	3.30	3.14	3.58	3.27	3.79	3.57	4.05	3.89	2.98
MnO	0.08	0.07	0.07	0.07	0.04	0.07	0.07	0.09	0.09	0.07
MgO	1.83	1.71	1.65	1.88	1.93	2.21	1.98	1.76	1.68	1.19
CaO	4.02	3.38	3.59	3.87	4.00	3.99	3.80	4.41	4.46	3.42
Na_2O	4.77	4.65	4.75	4.62	4.52	4.32	4.50	3.73	3.82	3.75
K_2O	1.96	2.54	2.13	2.36	2.84	2.28	2.44	2.48	2.55	3.22
P_2O_5	0.21	0.17	0.18	0.19	0.22	0.20	0.20	0.19	0.18	0.16
LOI	0.49	0.47	0.57	0.57	0.54	0.84	0.45	0.62	0.43	0.48
Total	100.34	99.91	99.76	99.45	99.91	100.68	99.95	99.51	99.45	99.70
A/CNK	0.99	0.99	0.99	0.97	0.94	0.96	0.97	1.00	0.98	1.01
T_{Zr} (°C)	801.2	802.7	817.3	793.6	790.3	785.6	810.6	781.0	786.5	806.1
Trace elements† (ppm)										
Ni	10.0	10.0	11.0	14.0	19.0	17.0	17.0	7.0	6.0	5.0
Cr	13.3	13.2	16.0	21.0	35.5	34.6	29.1	7.8	7.3	6.4
Sc	10.0	8.0	8.0	10.0	10.0	9.0	10.0	11.0	10.0	9.0
V	77.8	71.1	67.9	78.0	80.4	88.5	81.9	85.1	80.6	60.5
Ba	1198	1348	1199	1302	1240	1197	1277	1024	1067	1055
Rb	44	61	52	58	59	58	77	82	83	119
Sr	637	513	537	464	522	465	497	629	625	532
Zr	176	169	202	164	165	153	197	145	157	170
Y	13.9	12.6	14.6	13.1	12.2	13.7	12.0	15.1	15.5	13.2
Nb	5.9	6.3	7.4	10.2	7.5	9.7	6.8	7.0	7.0	8.2
Ga	20.4	20.8	20.4	19.7	19.5	19.0	20.9	19.9	19.1	19.5
Cu	15.4	25.6	19.8	9.0	3.4	48.1	24.1	11.0	9.2	8.9
Co	7.9	7.6	6.8	8.7	7.9	9.3	9.5	8.1	7.5	5.7
Zn	66.9	75.0	70.2	30.4	3.1	33.4	70.2	74.1	66.4	67.0
Pb	13.6	16.5	13.5	15.4	10.4	12.1	15.5	15.2	16.0	22.0
U	2.3	1.8	2.5	1.6	2.0	1.5	2.6	3.0	2.4	4.1
Th	8.6	8.9	8.7	10.2	9.9	9.4	10.4	9.2	8.3	13.3
Cs	0.9	0.9	1.3	0.7	2.6	1.1	2.0	2.8	2.5	3.0
Hf	3.7	3.6	4.3	4.2	4.2	4.0	4.2	3.2	3.5	4.0
Ta	0.6	0.7	0.7	0.7	0.6	0.7	0.6	0.8	0.9	1.0
La	21.0	22.1	25.9	22.7	25.5	23.6	25.1	22.2	23.3	24.8
Ce	41.6	42.0	48.6	45.1	47.2	46.6	45.6	41.9	44.0	46.0
Yb	1.10	0.99	1.20	1.61	2.02	1.55	0.85	1.28	1.34	1.13

Note: Major element concentrations are reported as weight percent (wt%) oxides and expressed as raw data; T_{Zr} (°C)—zircon saturation temperature after Watson and Harrison (1983). Bt.—biotite; Hbl.—hornblende.

*Major element analyses, Ni, and Sc by XRF (X-ray fluorescence) at Franklin and Marshall College.

†Trace element analyses (ppm) by inductively coupled plasma–mass spectrometry (ICP-MS) at Miami University.

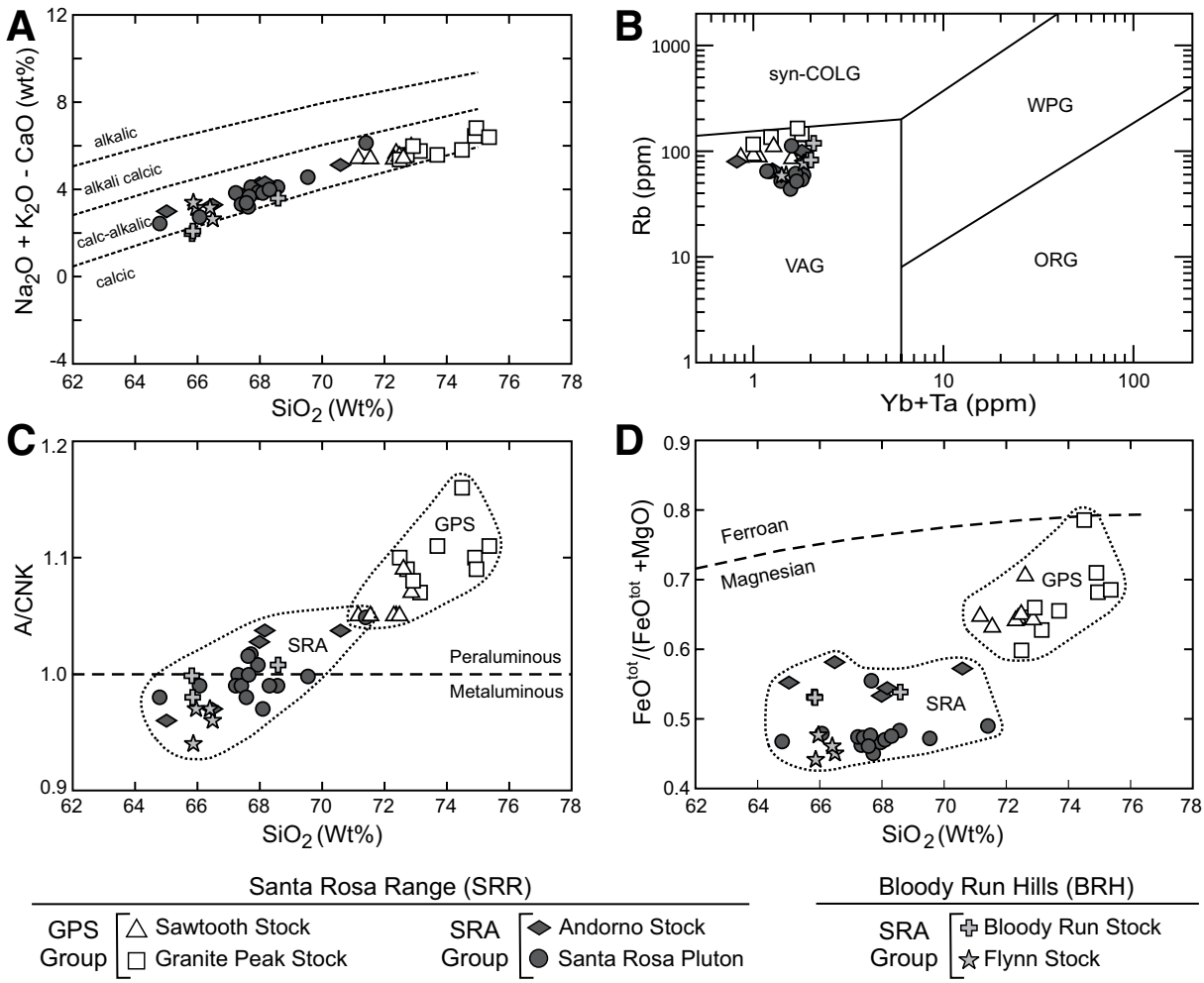

Figure 5. Various igneous classification plots for the Santa Rosa Range and Bloody Run Hills (SRR-BRH) granitoids. (A) Modified alkali-lime index versus SiO_2 (wt%) (after Frost et al., 2001). (B) Tectonic classification plot (Rb versus Yb + Ta) (after Pearce et al., 1984). ORG—ocean ridge granite; syn-COLG—syn-collisional granite; WPG—within plate granite; VAG—volcanic arc granite. (C) Aluminum saturation index (A/CNK) versus SiO_2 (wt%) (after Shand, 1969). Aluminum saturation index expressed as the molecular ratio of $Al_2O_3/(CaO + Na_2O + K_2O)$. (D) Fe* versus SiO_2 (wt%) (after Frost et al., 2001, and Miyashiro, 1974) [Fe* = $(FeO^{tot}/(FeO^{tot} + MgO)$; FeO^{tot} is total Fe]. All major and trace element analyses are reported in Table DR5.

high-Rb GPS granitoids. Upon closer examination, the bulk of the SRA group samples, notably the Santa Rosa pluton itself, display only a poorly defined positive relationship between Rb and silica, as compared to the well-defined and more rapid increase in Rb over a narrow range of silica for the GPS group. In the case of Ba, both groups display similar concentration ranges (SRA group ~1000–1500 ppm; GPS group ~1100–1700 ppm; Fig. 7) for the majority of samples, but the SRA group forms a cluster between ~65–70 wt% silica and the GPS group forms a separate cluster between 71 and 75 wt%. Only the most evolved samples from each group show distinct deviations in Ba concentrations.

Transition metal concentrations and their relationship with silica also define the SRA and GPS groups. The SRA granitoids contain a wide range of V concentrations that decrease with increasing silica (Fig. 7). The GPS granitoids show a similar pattern at much lower concentrations and over a more limited concentration range. The two groups are indicated by the offset/inflection in the V-silica arrays at ~71–72 wt% SiO_2, akin to the patterns depicted by MgO and Fe_2O_3.

High-field strength element versus silica plots also contain distinct offsets in the overall data trend around ~71–72 wt% SiO_2 and at the highest concentration of silica. In the Zr versus silica plot (Fig. 7), the SRA granitoids form a general trend of decreasing Zr with increasing silica, although an offset is noted between the main group of samples (~65–68 wt% SiO_2) and the highest silica samples that overlap with the GPS group. GPS granitoids maintain a fairly constant range of Zr (~100–150 ppm) until around ~74–76 wt% SiO_2, at which point, the concentration drops to 50–100 ppm. This abrupt drop at the highest silica end of the compositional spectrum is similar to that observed in other trace elements (e.g., Sr and Ba; Fig. 7). Both groups appear to form clusters rather than coherent trends in the Nb-silica plot. For example, when the high-silica samples (i.e., >70 wt% silica) in each of the SRA group intrusion are ignored, the majority of the SRA group samples form a cluster at ~65–68 wt% silica with a large range of Nb concentrations (~5–15 ppm). Similar groupings are also observed within individual intrusions of the GPS group, but are formed at higher silica concentrations (~72–74 wt% silica). The Sawtooth

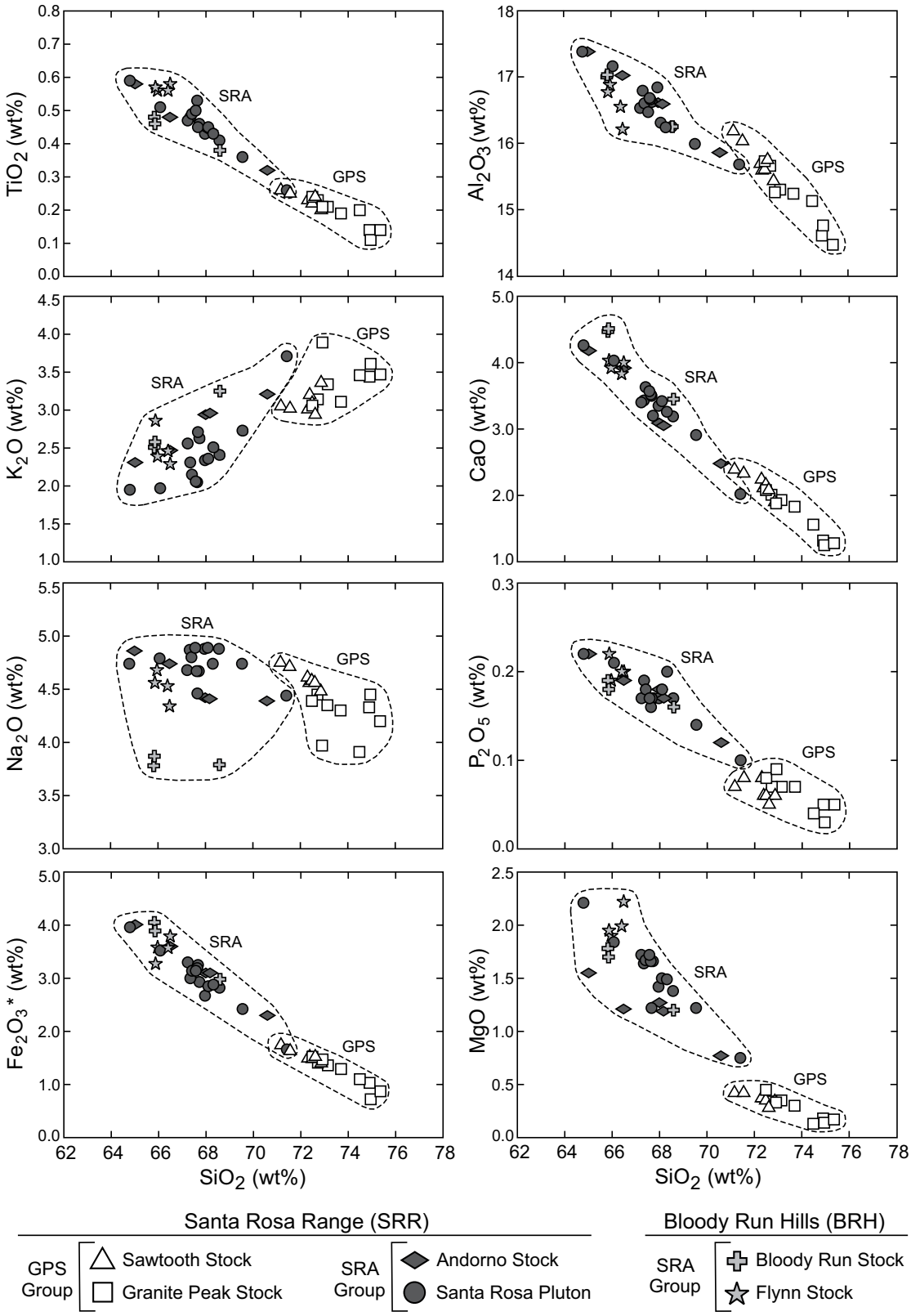

Figure 6. Major element chemical variation diagrams for the Santa Rosa Range and Bloody Run Hills (SRR-BRH) granitoids. Major elements are presented as weight percent oxide (wt%) and normalized to 100% anhydrous. Total Fe is presented as Fe_2O_3*. All major and trace element analyses are reported in Table DR5. SRA—Santa Rosa/Andorno group; GPS—Granite Peak/Sawtooth group.

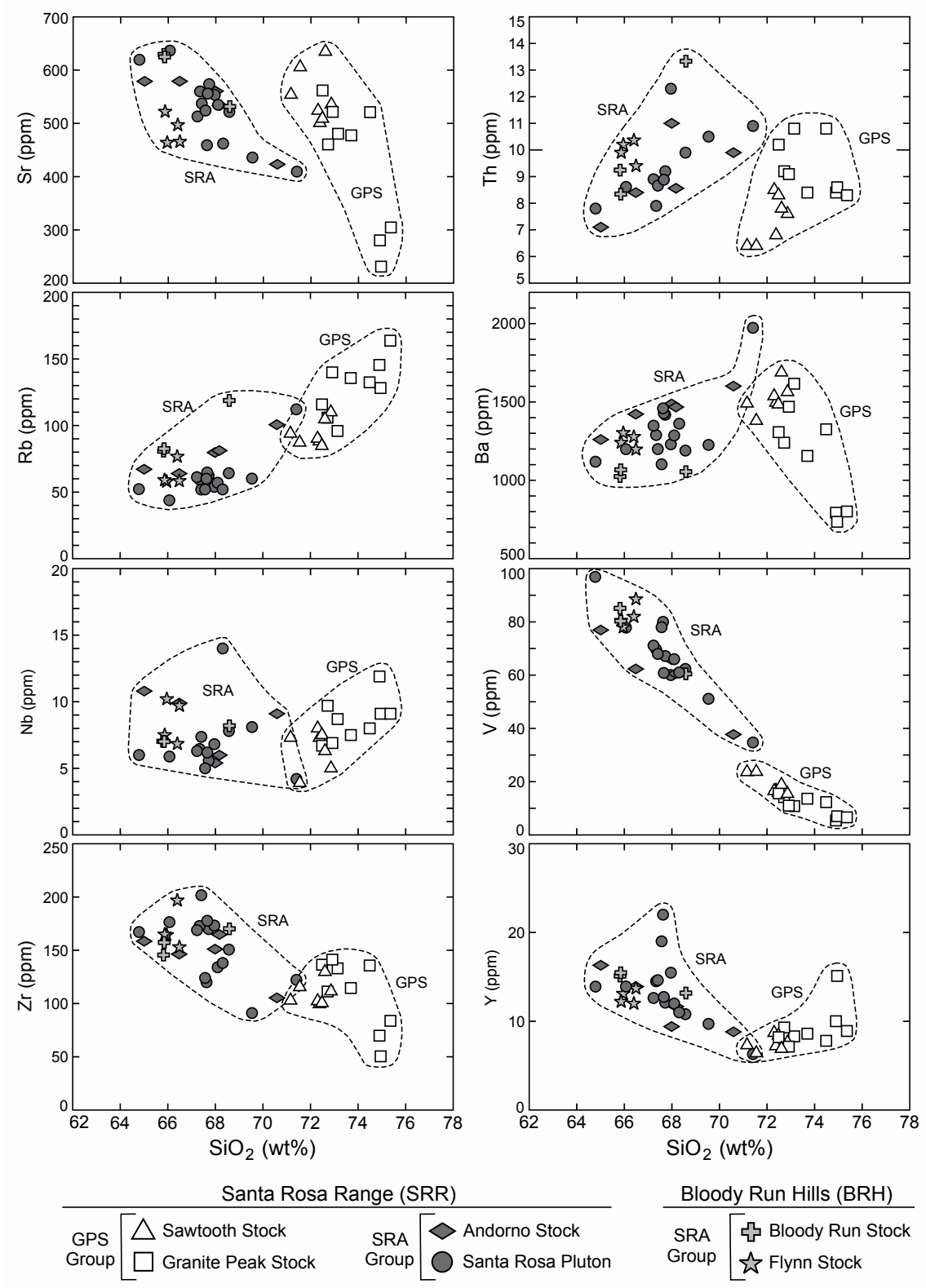

Figure 7. Chemical variation diagrams showing concentrations (in ppm) of selected trace elements versus SiO_2 (wt%) for the Santa Rosa Range and Bloody Run Hills (SRR-BRH) granitoids. All major and trace element analyses are reported Table DR5. SRA—Santa Rosa/Andorno group; GPS—Granite Peak/Sawtooth group.

TABLE 4. BULK ROCK Sr AND Nd ISOTOPE ANALYSES FOR THE SANTA ROSA RANGE AND BLOODY RUN HILLS GRANITOIDS

Sample	Intrusion	Age (Ma)*	Rb (ppm)†	Sr (ppm)†	Rb/Sr	Sm (ppm)†	Nd (ppm)†	Sm/Nd	$^{87}Sr/^{86}Sr$§	$^{143}Nd/^{144}Nd$§	εNd§	$^{87}Sr/^{86}Sr_{(i)}$#	$^{143}Nd/^{144}Nd_{(i)}$#	$εNd_{(T)}$#
KB11-05	Granite Peak	94.4 ± 1.6	106	460	0.23	2.88	15.7	0.18	0.706948	0.512428	–3.9	0.706054	0.512360	–2.9
RS91-8A	Granite Peak	94.4 ± 1.6	136	477	0.28	2.45	13.5	0.18	0.707180	0.512455	–3.4	0.706074	0.512387	–2.4
RS91-1A	Granite Peak	94.4 ± 1.6	164	305	0.54	2.32	11.7	0.20	0.708032	0.512436	–3.8	0.705945	0.512362	–2.9
CH-7	Granite Peak	94.4 ± 1.6	132	521	0.25	3.10	17.9	0.17	0.707120	0.512410	–4.3	0.706137	0.512345	–3.2
RS91-33	Sawtooth	92.5 ± 1.2	87	605	0.14	2.36	14.0	0.17	0.706170	0.512495	–2.6	0.705623	0.512433	–1.5
RS91-37	Sawtooth	92.5 ± 1.2	110	536	0.21	2.65	15.1	0.18	0.706607	0.512456	–3.4	0.705827	0.512392	–2.3
CH-15A	Sawtooth	92.5 ± 1.2	105	634	0.17	2.63	15.2	0.17	0.706520	0.512498	–2.6	0.705890	0.512435	–1.8
RS91-40B	Andorno	100.7 ± 1.1	80	560	0.14	3.05	16.1	0.19	0.705464	0.512617	–0.3	0.704873	0.512542	0.8
KB11-20	Andorno	100.7 ± 1.1	67	579	0.12	4.67	21.5	0.22	0.705301	0.512629	–0.2	0.704822	0.512543	0.8
KB11-25	Santa Rosa	102.1 ± 1.2	60	436	0.14	2.89	14.8	0.19	0.705058	0.512690	1.2	0.704480	0.512611	2.2
RS91-19	Santa Rosa	102.1 ± 1.2	112	409	0.27	2.78	16.6	0.17	0.705910	0.512664	0.7	0.704761	0.512596	1.9
RS91-24A	Santa Rosa	102.1 ± 1.2	52	619	0.08	4.00	20.5	0.19	0.704530	0.512697	1.3	0.704177	0.512618	2.3
RS91-28A	Santa Rosa	102.1 ± 1.2	64	522	0.12	3.16	16.8	0.19	0.704560	0.512696	1.3	0.704045	0.512620	2.4
RS91-42	Bloody Run	96.1 ± 1.3	83	625	0.13	4.49	18.0	0.25	0.705757	0.512495	–2.6	0.705232	0.512400	–2.1
RS91-43	Bloody Run	96.1 ± 1.3	119	532	0.22	4.03	18.8	0.21	0.706309	0.512462	–3.3	0.705425	0.512381	–2.5
KB11-09	Flynn	104.6 ± 1.3	58	464	0.12	4.06	18.9	0.21	0.704935	0.512712	1.6	0.704398	0.512623	2.5
KB11-28	Flynn	104.6 ± 1.3	58	465	0.13	4.45	20.6	0.22	0.705040	0.512675	0.9	0.704504	0.512586	1.8

*Weighted mean U-Pb age determined by laser-ablation inductively coupled plasma–mass spectrometry (LA-ICP-MS); (± 2σ uncertainty).
†Elemental concentrations were determined by ICP-MS; concentrations have a <2% error on all reported values.
§2σ external reproducibility - $^{87}Sr/^{86}Sr$= 0.000017; $^{143}Nd/^{144}Nd$ = 0.000008; εNd = 0.3.
$^{87}Sr/^{86}Sr_{(i)}$, $^{143}Nd/^{144}Nd_{(i)}$, and $εNd_{(T)}$ are age corrected to the age of the intrusion.

stock, for example, forms a cluster of Nb concentrations (~4–8 ppm) over a narrow silica range (~71–73 wt%). The Granite Peak samples form a similar cluster, but at higher Nb (~6–12 ppm) and silica (~72–75 wt%).

The yttrium versus silica plot also highlights the two distinct granitoid groups (Fig. 7). Although some or all samples from individual intrusions define coherent trends (e.g., Santa Rosa pluton, Andorno stock), the SRA and GPS groups tend to form distinct groupings when the high-silica outliers are ignored. The majority of the SRA group samples form a cluster at ~65–68 wt% silica, while the majority of the GPS group samples cluster around 72–74 wt% silica.

Synthesis of Bulk Rock Major and Trace Element Geochemistry

The SRR-BRH granitoids include compositions ranging from quartz monzodiorite to granite, spanning a range in SiO_2 from ~64–76 wt% (Fig. 3). The observed mineralogies change systematically within this silica range. Hornblende and sphene are present in the lower silica compositions (<70 wt% SiO_2), whereas trace muscovite and rare garnet are restricted to peraluminous, high-silica granitoids (Table 1; Fig. 3).

Bulk major and trace element data further emphasize the SRA and GPS granitoid groups. The observed chemical variations between the two groups suggest that they are not related to a common source or set of petrogenetic processes. In general, the older SRA granitoids are more mafic (~64–71 wt% SiO_2), metaluminous, and dominated by hornblende-bearing granodiorites (Figs. 5–7; Table 3). Comparatively, the younger GPS granitoids are more felsic (~71–76 wt% SiO_2), peraluminous, and consist primarily of biotite granites-granodiorites. These data indicate a broad compositional shift from more mafic and metaluminous to felsic and peraluminous magmatism with time in the SRR-BRH region.

ISOTOPE GEOCHEMISTRY

Bulk Rock Sr and Nd Isotope Data

A suite of seventeen samples from the six SRR-BRH intrusions was selected for Sr and Nd isotope analyses. Analytical methods for these analyses are described in the Data Repository Item. Elemental concentrations, measured isotope values, and age corrected isotope values are reported in Table 4. All reported initial $^{87}Sr/^{86}Sr$ ratios and $εNd_{(t)}$ values are age corrected to the age of the intrusion (Fig. 4 and Table 4).

Initial $^{87}Sr/^{86}Sr$ ratios of the SRR-BRH granitoids show considerable variability, ranging from 0.7040 to 0.7061 (Fig. 8). Within this range, the two defined granitoid groups are clearly distinguished. The older, more mafic SRA group is characterized by less radiogenic initial $^{87}Sr/^{86}Sr$ ratios (0.7040–0.7054), and the younger, more felsic GPS group by higher initial $^{87}Sr/^{86}Sr$ ratios (0.7056–0.7061).

Comparable variability in the $εNd_{(t)}$ values is also observed, ranging from –3.2 to +2.5 (Fig. 8). With the exception of the Bloody Run stock,

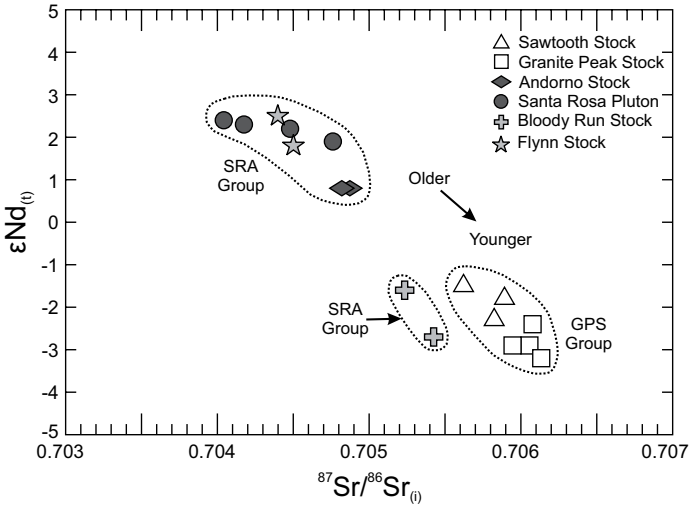

Figure 8. Bulk Rock $εNd_{(t)}$ versus $^{87}Sr/^{86}Sr_{(i)}$ isotope plot for the Santa Rosa Range and Bloody Run Hills (SRR-BRH) granitoids. $εNd_{(t)}$ and $^{87}Sr/^{86}Sr_{(i)}$ values are age corrected to the U-Pb age of each intrusion (see Table 4; Fig. 4). Bulk rock Sr and Nd isotope data and elemental concentrations are reported in Table 4. 2σ external reproducibility: $^{87}Sr/^{86}Sr$ = 0.000017; $^{143}Nd/^{144}Nd$ = 0.000008; εNd = 0.3. SRA—Santa Rosa/Andorno group; GPS—Granite Peak/Sawtooth group.

TABLE 5. WEIGHTED MEAN Hf ISOTOPE AND U-Pb DATA FOR THE SANTA ROSA RANGE AND BLOODY RUN HILLS GRANITOIDS

Sample ID*	N	Avg. (^{176}Yb + ^{176}Lu)/^{176}Hf (%)	^{176}Hf/^{177}Hf *	± (2σ)	^{176}Lu/^{177}Hf *	± (2σ)	^{176}Hf/^{177}Hf$_{(T)}$†	εHf$_{(T)}$†	± (2σ)	U-Pb age (Ma)§	± (2σ)§
Santa Rosa pluton											
RS91-24A	10	9.4	0.282844	0.000025	0.0006	0.0002	0.282843	4.3	1.8	102.1	1.2
KB11-25	8	18.5	0.282862	0.000030	0.0014	0.0004	0.282859	4.9	2.0	102.1	1.2
RS91-19	8	18.3	0.282860	0.000025	0.0013	0.0003	0.282858	4.8	1.8	102.1	1.2
Andorno stock											
RS91-40B	4	20.0	0.282826	0.000046	0.0015	0.0005	0.282823	3.6	3.3	100.7	1.1
KB11-20	6	19.9	0.282805	0.000036	0.0013	0.0005	0.282803	2.9	2.6	100.7	1.1
Granite Peak stock											
RS91-8A	8	13.9	0.282664	0.000034	0.0009	0.0005	0.282662	–2.2	2.4	94.4	1.6
KB11-05	5	11.3	0.282623	0.000039	0.0007	0.0005	0.282622	–3.7	2.8	94.4	1.6
Sawtooth stock											
RS91-33	8	19.7	0.282743	0.000027	0.0012	0.0005	0.282741	0.5	1.9	92.5	1.2
RS91-37	5	20.9	0.282713	0.000038	0.0013	0.0004	0.282711	–0.6	2.6	92.5	1.2
Flynn stock											
KB11-09	8	9.5	0.282872	0.000030	0.0006	0.0002	0.282872	5.4	2.2	104.6	1.3
Bloody Run stock											
RS91-42	6	10.6	0.282714	0.000029	0.0008	0.0004	0.282713	–0.4	2.0	96.1	1.3

*Individual zircon Hf isotope analyses are presented in Table DR6 (see text footnote 1).
†^{176}Hf/^{177}Hf$_{(T)}$ and εHf$_{(T)}$ values are age corrected to the intrusion U-Pb age reported in this table.
§Intrusion U-Pb age and 2σ uncertainty.

the older SRA group is characterized by more positive εNd$_{(t)}$ values (+0.8 to +2.5) than the younger GPS group (−3.2 to −1.5).

The Bloody Run stock has initial ^{87}Sr/^{86}Sr ratios (0.7052 and 0.7054) and εNd$_{(t)}$ values (−2.1 and −2.5) more consistent with the GPS group, but is compositionally more similar to the SRA granitoids.

Zircon Hf Isotopic Data

Hafnium isotope compositions of zircons were measured on top of spots previously excavated for U-Pb analyses using LA-MC-ICP-MS. This directly ties the Hf isotope measurement to a zircon U-Pb age. Analytical methods for the Hf isotope analyses are described in the Data Repository Item. Approximately five to ten Hf isotope measurements were collected on autocrystic zircon rims for each of the eleven samples previously analyzed for U-Pb geochronology. Because autocrystic zircon grains are interpreted to crystallize from the surrounding melt, their rim compositions are interpreted to reflect the Hf isotope composition of the melt during the crystallization of the zircon. Using individual rim analyses, a single pooled weighted mean ^{176}Hf/^{177}Hf value was determined to characterize the Hf isotope composition of the melt for each intrusion. The weighted mean values are reported in Table 5 and individual Hf isotope analyses used to construct the pooled weighted mean values are presented in Table DR6. All Hf isotope compositions are age corrected to the U-Pb age of the intrusion and are reported as ^{176}Hf/^{177}Hf$_{(t)}$ and εHf$_{(t)}$ in Table 5. Fig. 9 is a plot of age versus the weighted mean εHf$_{(t = \text{age of intrusion})}$ value for the six SRR-BRH granitoid intrusions.

Although a single bulk sample may display variability in its zircon εHf$_{(t)}$ values (e.g., RS91-24A, εHf$_{(t)}$ = +2.1 to +6.0, Table DR6), a consistent pattern of decreasing εHf$_{(t)}$ with time is observed among the SRR-BRH intrusions. This pattern is also reflected in the pooled weighted mean values, revealing a nearly continuous trend that ranges from +5.4 to −3.7 (Fig. 9). The granitoid groups are clearly evident within this overall trend. The older, more mafic SRA group is generally defined by higher initial εHf values (+2.9 to +5.4, excluding the Bloody Run stock) and the younger, more felsic GPS group is defined by granitoids with less radiogenic εHf values (−3.7 to +0.5). Despite having a similar bulk chemistry and modal mineralogy to the SRA group, the Bloody Run stock has an εHf$_{(t)}$ value (−0.4) more consistent with the GPS group. Because the Bloody Run stock has an age intermediate between the two granitoid pulses, it may represent an important transitional magmatic pulse that shares characteristics

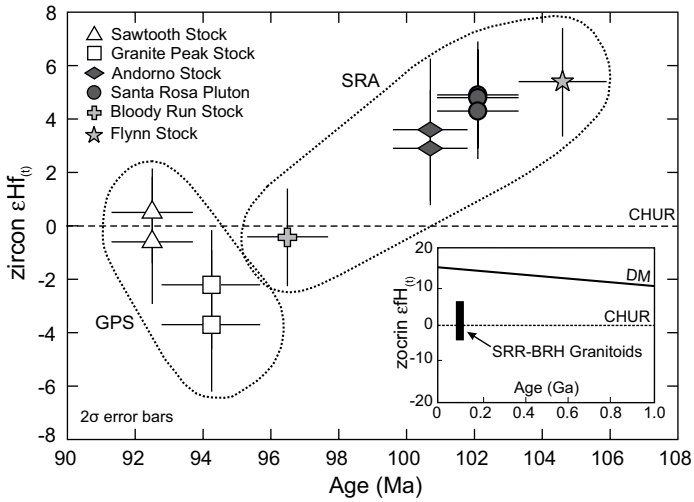

Figure 9. Plot showing zircon εHf$_{(t)}$ zircon values versus intrusion age (Ma) for the Santa Rosa Range and Bloody Run Hills (SRR-BRH) granitoids. All εHf$_{(t)}$ values shown are age corrected to the intrusion age (see Table 5; Fig. 4). Zircon rim Hf isotope analyses were pooled for each of the eleven SRR-BRH samples (Table DR6). A single weighted mean εHf$_{(t)}$ value was calculated for each sample using the pooled analyses (Table 5). Calculations were done using routines in Isoplot (Ludwig, 2008). Each symbol represents the calculated weighted mean εHf$_{(t = \text{age of intrusion})}$ value for pooled analyses from each sample. Dashed horizontal line represents expected εHf$_{(t)}$ for CHUR (chondritic uniform reservoir). Error bars are shown at the 2σ level. Insert (lower right) shows where zircon data plot on expanded εHf$_{(t)}$ versus age diagram relative to depleted mantle (DM) and CHUR.

common to both groups. The transitional character of the Bloody Run stock is also apparent in the bulk Sr and Nd isotope data (Fig. 8).

Xenocrystic zircon cores were analyzed in order to characterize potential source materials and assimilants. These data are summarized in Table 6 and shown in Fig. DR4B. Populations of xenocrystic zircon cores with variable $\varepsilon Hf_{(t = U\text{-}Pb\ zircon\ age)}$ isotope values (+8.6 to −22.2) and U-Pb ages (ca. 250 Ma to >1 Ga) were identified in all of the SRR intrusions (Table 6). As stated earlier, BRH intrusions also have xenocrystic cores (i.e., U-Pb ages >100 Ma). However, Hf isotope compositions were not measured on these cores because the core regions are too small to precisely measure with the LA-MC-ICP-MS spot size (40 microns). Thus, we focus only on the U-Pb ages and Hf isotope compositions of the xenocrystic zircon cores from the SRR intrusions.

With the exception of one xenocrystic core (ca. 1942 Ma, $\varepsilon Hf_{(t)} = -5.4$), the Andorno stock generally forms a cluster (ca. 1000–1150 Ma; $\varepsilon Hf_{(t)} = -0.4$ to +8.6) (Table 6). Xenocrystic cores from the Sawtooth stock yield similar U-Pb ages and Hf isotope compositions (ca. 1043 Ma, $\varepsilon Hf_{(t)} = -0.2$; ca. 926 Ma, $\varepsilon Hf_{(t)} = 0.7$). The Santa Rosa pluton contains a diverse population of xenocrystic core U-Pb ages (ca. 249 Ma, ca. 1471 Ma, ca. 1974 Ma) and $\varepsilon Hf_{(t)}$ values (−1.6, +5.3, −22.2, respectively). A xenocrystic core from the Granite Peak stock yields a U-Pb age of ca. 447 Ma and has a $\varepsilon Hf_{(t)}$ value of −12.1 (Table 6). The implications of these xenocrystic zircon cores are discussed in the following section.

Synthesis of Bulk Sr and Nd Isotopes and Zircon Hf Isotopes

Bulk Sr and Nd and zircon Hf isotope analyses provide a more complete view of magmatism in this region. The older, more mafic SRA granitoids possess initial $^{87}Sr/^{86}Sr$ and εNd isotope values that reveal a significant mantle contribution (i.e., 0.7040–0.7048; +0.8 to +2.5). Juvenile zircon $\varepsilon Hf_{(t = age\ of\ intrusion)}$ values (+2.9 to +5.4) and higher concentrations of TiO_2, MgO, Fe_2O_3, CaO, and transition metals (V, Sc, Cr, Ni) support this interpretation. Other intrusions within western Nevada share similar bulk compositions and isotopic values. Van Buer and Miller (2010) reported a narrow range of initial $^{87}Sr/^{86}Sr$ values around 0.7047 and εNd values around −0.2 for a suite of nested intrusions within the Sahwave Range. These intrusions were interpreted to be generated from a relatively homogeneous source dominated by a mantle component. Previous regional studies reported similar Sr and Nd isotope values, concluding that granitic intrusions west of the initial $^{87}Sr/^{86}Sr = 0.706$ isopleth (Fig. 1) are dominated by juvenile, mantle-derived materials that progressively exhibit greater contributions from evolved, presumably cratonic crustal sources toward the east (Farmer and DePaolo, 1983; Elison et al., 1990; Wright and Wooden, 1991; Wooden et al., 1999).

Comparatively, the younger, more felsic GPS intrusions preserve initial isotope values that indicate a greater crustal influence (initial $^{87}Sr/^{86}Sr = 0.7056–0.7061$; $\varepsilon Nd_{(t)}$ values = −1.5 to −3.2; $\varepsilon Hf_{(t)} = +0.5$ to −3.7). This interpretation is supported by the peraluminous character, high K_2O and Rb, and higher Rb/Sr ratio (0.2–0.6) than the SRA granitoids (<0.2). These isotope signatures are more consistent with intrusions formed along the North American continental margin (e.g., Tuolumne Intrusive Suite: $^{87}Sr/^{86}Sr_{(i)} = 0.7056–0.7073$, $\varepsilon Nd_{(t)} = -3$ to −8; Gray et al., 2008). Coincident with the change in bulk elemental compositions, the shift in isotope compositions (Sr, Nd, and Hf) indicates that the relative importance of mantle and crustal contributions changed systematically over the time span from ca. 105 to 92 Ma. The close spatial association of the two geochemically and isotopically distinct granitoid groups is quite surprising and suggests that magmatism in this region contains previously undocumented temporal and compositional complexities. Although broad secular variations have been investigated for intrusions throughout the Basin and Range Province (e.g., Wright and Wooden, 1991), such variations have not been previously documented at this spatial scale within northwestern Nevada.

TABLE 6. ZIRCON Hf ISOTOPE ANALYSES—XENOCRYSTIC CORE AND AUTOCRYSTIC RIM PAIRS

Sample name	Spot location	$(^{176}Yb + ^{176}Lu)/^{176}Hf$ (%)	$^{176}Hf/^{177}Hf$*	$^{176}Lu/^{177}Hf$	$^{176}Hf/^{177}Hf_{(T)}$†	$\varepsilon Hf_{(T)}$†	± (2σ)	$^{206}Pb/^{238}U$ (Ma)	± (2σ)
Granite Peak stock									
RS91-8A-4-19R	Rim	23.4	0.282711 (35)	0.001327	0.282708	–0.6	1.2	93.8	1.6
RS91-8A-4-18C	Core	10.5	0.282167 (43)	0.000749	0.282160	–12.1	1.6	447.1	9.4
Sawtooth stock									
RS91-33-3-5R	Rim	15.4	0.282765 (49)	0.000880	0.282763	1.3	1.7	92.4	2.3
RS91-33-3-6C	Core	13.5	0.282132 (71)	0.000742	0.282118	–0.2	2.5	1043.6	41.5
RS91-37-7-11R	Rim	16.1	0.282724 (36)	0.001044	0.282722	–0.2	1.3	91.9	3.1
RS91-37-7-12C	Core	6.5	0.282225 (38)	0.000347	0.282219	0.7	1.4	926.4	12.7
Andorno stock									
KB11-20-1-1R	Rim	9.6	0.282795 (48)	0.000605	0.282794	2.6	1.7	104.6	3.4
KB11-20-1-2C	Core	5.5	0.282143 (37)	0.000286	0.282138	–0.4	1.3	1005.7	55.1
KB11-20-1-3R	Rim	19.4	0.282765 (46)	0.001506	0.282762	1.5	1.6	102.3	1.2
KB11-20-1-4C	Core	11.5	0.282317 (45)	0.000895	0.282297	8.6	1.6	1153.2	45.2
KB11-20-3-11R	Rim	22.5	0.282816 (39)	0.001423	0.282813	3.2	1.4	100.5	1.7
KB11-20-3-12C	Core	13.2	0.282283 (52)	0.000690	0.282269	5.4	1.9	1054.6	12.0
KB11-20-4-17R	Rim	14.8	0.282836 (50)	0.000953	0.282834	4.0	1.8	101.7	0.9
KB11-20-4-18C	Core	30.8	0.281455 (58)	0.001673	0.281393	–5.4	2.1	1942.0	35.1
Santa Rosa pluton									
RS91-24A-2-10R	Rim	5.0	0.282805 (39)	0.000335	0.282804	3.0	1.4	104.4	5.4
RS91-24A-2-9C	Core	0.7	0.280899 (42)	0.000032	0.280897	–22.2	1.5	1974.0	23.0
RS91-24A-4-20C	Core§	17.0	0.282026 (93)	0.000971	0.281999	5.3	3.3	1471.1	26.6
RS91-19-11-43C	Core§	8.8	0.282587 (67)	0.000611	0.282584	–1.6	2.4	249.5	11.8

*Numbers in parentheses are 2σ analytical uncertainties.
†$^{176}Hf/^{177}Hf_{(T)}$ and $\varepsilon Hf_{(T)}$ values are age corrected to the $^{206}Pb/^{238}U$ zircon age (Ma) reported in this table.
§These cores are not associated with autocrystic rim analyses.

Variable Hf isotope compositions ($\varepsilon Hf_{(t = \text{U-Pb zircon age})}$ = +8.6 to −22) from xenocrystic zircon cores indicate that older crustal components were involved in the petrogenesis of all of the SRR magmas (Fig. 10; Brown and Hart, 2013); previous studies have not reported evidence of ancient crustal reservoirs in this region. A comparison of xenocrystic zircon U-Pb ages from the SRR-BRH intrusions (n = 64) to the ages of Cordilleran basement provinces suggests diverse basement contributions, spanning much of the southwestern U.S. (Fig. 10A). Because there are no exposures of basement rocks in this region with comparable ages, the large variability of xenocrystic zircon U-Pb ages suggests that the origin is likely from a sedimentary source. To evaluate this hypothesis, xenocrystic zircon core U-Pb ages and $\varepsilon Hf_{(t = \text{U-Pb zircon age})}$ values are compared to detrital zircon data recently reported for sedimentary units in the Cordillera (Gehrels and Pecha, 2014). As shown in Figure 10B, the U-Pb ages and Hf isotope compositions of SRR xenocrystic zircon cores are strikingly similar to patterns of detrital zircons from Triassic sedimentary units within Nevada and Utah (Chinle and Osobb Formations; Gehrels and Pecha, 2014). The temporal and isotopic similarities suggest that local sedimentary units may be the origin of these xenocrystic zircon cores and a potential source of crustal contamination in the SRR magmas.

DISCUSSION

Continuity of the Cretaceous Magmatic Arc in Northwestern Nevada

Although widespread Cenozoic volcanism and faulting within the present-day Basin and Range Province obscures much of the earlier Mesozoic relationships, several studies have argued that the Cretaceous magmatic arc was continuous throughout northwestern Nevada and southwestern Idaho (e.g., Smith et al., 1971; Barton et al., 1988. Van Buer et al., 2009; Van Buer and Miller, 2010; Benford et al., 2010). Based on petrography, bulk elemental analyses, and K/Ar ages, Smith et al. (1971) concluded that granitoid intrusions within northwestern Nevada (termed the Lovelock Intrusive epoch, ca. 105–85 Ma) are indistinguishable from granitic intrusive suites within the Sierra Nevada and Idaho batholiths. More recently,

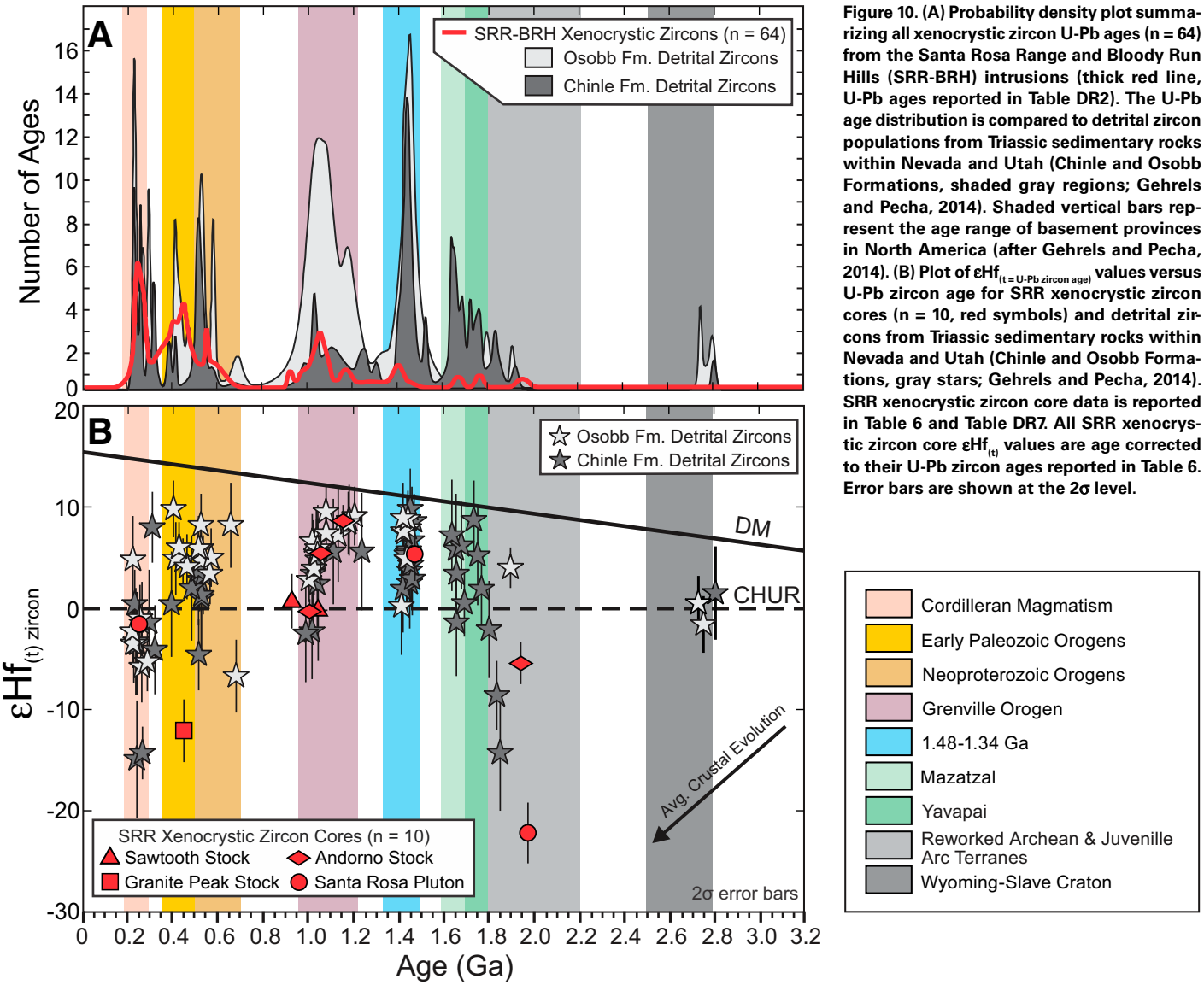

Figure 10. (A) Probability density plot summarizing all xenocrystic zircon U-Pb ages (n = 64) from the Santa Rosa Range and Bloody Run Hills (SRR-BRH) intrusions (thick red line, U-Pb ages reported in Table DR2). The U-Pb age distribution is compared to detrital zircon populations from Triassic sedimentary rocks within Nevada and Utah (Chinle and Osobb Formations, shaded gray regions; Gehrels and Pecha, 2014). Shaded vertical bars represent the age range of basement provinces in North America (after Gehrels and Pecha, 2014). (B) Plot of $\varepsilon Hf_{(t = \text{U-Pb zircon age})}$ values versus U-Pb zircon age for SRR xenocrystic zircon cores (n = 10, red symbols) and detrital zircons from Triassic sedimentary rocks within Nevada and Utah (Chinle and Osobb Formations, gray stars; Gehrels and Pecha, 2014). SRR xenocrystic zircon core data is reported in Table 6 and Table DR7. All SRR xenocrystic zircon core $\varepsilon Hf_{(t)}$ values are age corrected to their U-Pb zircon ages reported in Table 6. Error bars are shown at the 2σ level.

Colgan et al. (2006) argued that the isolated intrusions of the western Basin and Range share similar compositions, ages, exposure levels, and metamorphic assemblages to the Sierra Nevada batholith, suggesting that this region was contiguous during the Late Cretaceous. Van Buer and Miller (2010) concluded that the Sahwave and Nightingale Ranges of northwestern Nevada share similar ages, petrology, and compositions to the large concentrically zoned Late Cretaceous intrusive suites of the Sierra Nevada batholith. A seismic refraction/reflection/teleseismic study across the northern Basin and Range Province also documented a nearly 100-km-wide zone of low upper-crustal velocities, consistent with tonalitic to granitic rocks down to a depth of ~15 km (Lerch et al., 2007). A paleogeologic map reconstruction of northwestern Nevada also demonstrated that the Sierra Nevada batholith was continuous to the northeast across the Basin and Range (Van Buer et al., 2009). Additionally, Benford et al. (2010) examined several isolated intrusions within the Owyhee Mountains of southwestern Idaho. Geochronologic, structural, and isotopic analyses of these intrusions reveal similar ages, deformation histories, and initial $^{87}Sr/^{86}Sr$ isotope gradients comparable to the western Idaho shear zone (WISZ) of the Idaho batholith. Based on these results, they interpreted these intrusions to be the southern continuation of the WISZ and the Idaho batholith south of the Snake River Plain (Benford et al., 2010).

Owing to the high density of exposed plutonic rocks (>50%) and pervasive low- to medium-grade metamorphism (greenschist to amphibolite) within the western Great Basin, Barton et al. (1988) argued that western Nevada resembles the plutonic terrane of the Sierra Nevada Mountains. Directly east, intrusion density decreases, giving way to isolated intrusions that characterize much of the basinal and shelf terranes of western Nevada (Fig. 2). As this study is the first detailed study of magmatism within this low-intrusion density region, it provides a more comprehensive view of magmatism near the initial $^{87}Sr/^{86}Sr = 0.706$ isopleth in western Nevada (Fig. 1). In the following section, we focus on the broad similarities of magmatism in this region relative to the neighboring arc systems. Within this discussion, we emphasize the continuity of the Cretaceous magmatic arc in northwestern Nevada.

The SRR-BRH in Cordilleran Context

The timing of magmatism and the geochemical similarities of the SRR-BRH intrusions to the neighboring arc segments argue that these isolated intrusions were associated with the Late Cretaceous flare-up event that impacted the large batholithic systems. A compilation of recently published geochronology confirms that the isolated intrusions of the SRR-BRH are broadly coeval with other Cretaceous magmatic suites/events (Fig. 11). The ca. 105–92 Ma SRR-BRH intrusions are temporally coincident with the following regional magmatic pulses: (1) the Sierra Crest Magmatic Event of the Sierra Nevada batholith (ca. 98–86 Ma, Coleman and Glazner, 1997);

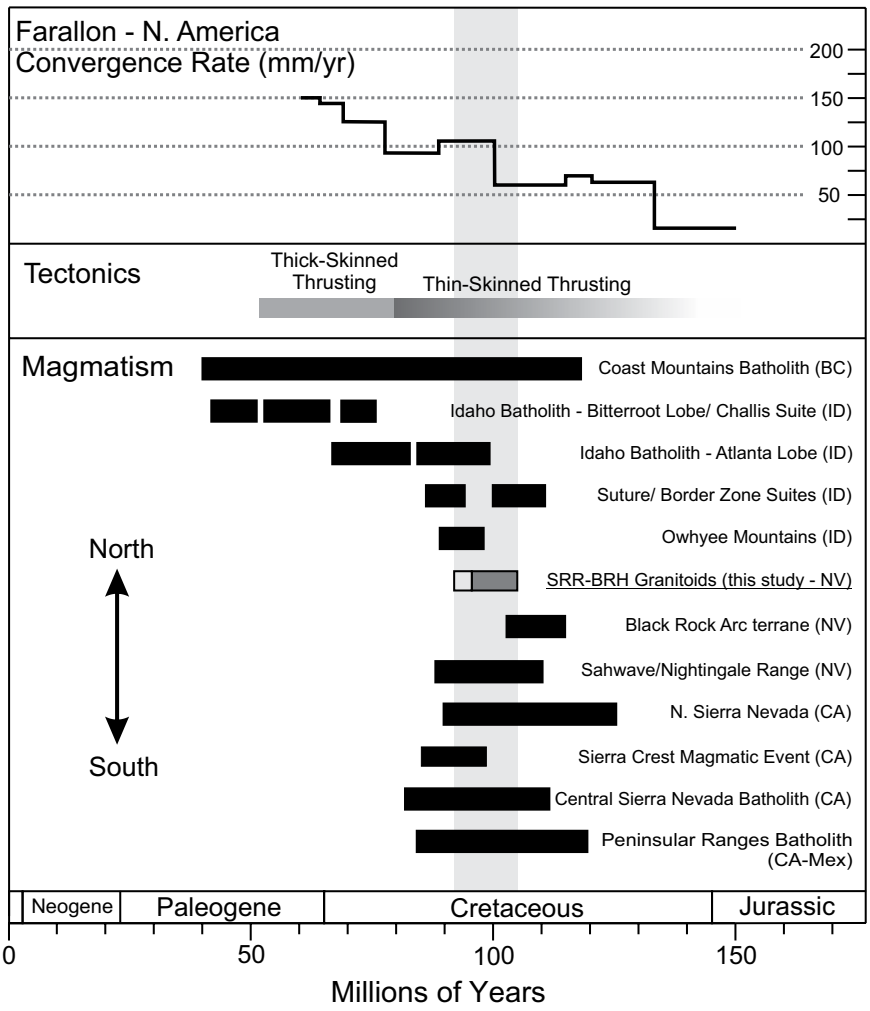

Figure 11. Compilation of magmatic and tectonic events within the North American Cordillera. (Top) Summary of Farallon–North America convergence rates after DeCelles (2004). (Middle) Timing of Cordilleran tectonic regimes (Thin-Skinned Thrusting—Sevier Style; Thick-skinned Thrusting—Laramide Style) after Gaschnig et al. (2010). (Bottom) Timing of Cordilleran magmatic pulses after Gaschnig et al. (2010). The SRR-BRH granitoids are shown in dark gray (SRA group) and light gray (GPS group). Ages compiled from Bateman (1992), Coleman and Glazner (1997), Ciavarella and Wyld (2008), Gehrels et al. (2009), Benford et al. (2010), Gaschnig et al. (2010), Van Buer and Miller (2010), Cecil et al. (2011, 2012), and Gaschnig et al. (2017). The vertical gray bar highlights the timing of SRR-BRH magmatism with respect to other Cordilleran events. The Sierra Crest magmatic event of Coleman and Glazner (1997) is also shown for comparison.

(2) the suture zone suite of the Salmon River suture zone (ca. 125–90 Ma, Giorgis et al., 2008; Gaschnig et al., 2010); (3) the early metaluminous suite of the Idaho batholith (ca. 100–85 Ma, Gaschnig et al., 2010, 2017); (4) intrusions of the Sahwave and Nightingale Ranges of northwestern Nevada (ca. 110–89 Ma, Van Buer and Miller, 2010); and (5) the isolated intrusions of the Owyhee Mountains (ca. 98–90 Ma, Benford et al., 2010).

Broad geochemical similarities between the SRR-BRH intrusions and the neighboring batholith systems suggest that the SRR-BRH intrusions were formed in a similar continental magmatic arc setting. As illustrated in Figure 12, the SRR-BRH intrusions have MORB-normalized trace element patterns very similar to granitoid intrusions emplaced in California (e.g., Tuolumne, Gray et al., 2008; northern Sierra Nevada intrusions, Cecil et al., 2012), western Nevada (Sahwave intrusive suite, Van Buer and Miller, 2010), and Idaho (metaluminous and peraluminous suites of the Idaho batholith–Atlanta Lobe, Gaschnig et al., 2011). However, unlike the larger batholiths that were emplaced in or along thick North American lithosphere, the SRR-BRH granitoids were emplaced in thick metasedimentary packages, presumably underlain by transitional lithosphere (e.g., Van Buer and Miller, 2010). Therefore, these broad geochemical similarities suggest that common processes or source regions were responsible for the formation of arc magmatism along a substantial portion of the Cretaceous arc system (ca. 110–85 Ma). This observation warrants a more thorough investigation, one that requires additional data sets beyond the scope of this paper.

Eastward migrations in arc magmatism have been documented in many of the Cordilleran arcs during Early to Late Cretaceous time (e.g., Coleman and Glazner, 1997; Lackey et al., 2005; Gehrels et al., 2009; Lackey et al., 2012; Morton et al., 2014; Ducea et al., 2015a, 2015b; Paterson and Ducea, 2015). Within the Sierra Nevada batholith, magmatism migrated eastward, leading to the construction and emplacement of the iconic zoned intrusions of the Sierra Crest magmatic event (e.g., Tuolumne Intrusive Suite, ca. 95–85 Ma; Coleman and Glazner, 1997; Coleman et al., 2004). To the north, intrusions of the Salmon River suture zone (ca. 110–100 Ma) along the west edge of the Idaho batholith formed a poorly defined west to east, mafic to felsic plutonic suite (Gaschnig et al., 2017). Between 105 and 92 Ma, transpressional deformation transformed these intrusions into a suite of orthogneisses along the western Idaho shear zone (WISZ) (Giorgis et al., 2008; Gaschnig et al., 2017). Coincident with this period of deformation, Idaho batholith magmatism shifted eastward, forming the border zone and early metaluminous suites (ca. 98–85 Ma; Gaschnig et al., 2011; 2017). Gaschnig et al. (2011) argued that the age, geochemistry, and isotopic signatures of these magmatic phases are reminiscent of flare-up events recorded in the Sierra Nevada and Peninsular Ranges batholiths, and were likely continuous throughout northwestern Nevada.

Recent U-Pb zircon geochronology of intrusions within northwestern Nevada has defined emplacement ages ranging from ca. 116–92 Ma (Wyld, 2000; Wyld et al., 2001; Wyld and Wright, 2005; Colgan et al., 2006; this study). Ciavarella and Wyld (2008) indicate that the intrusions of the Black Rock arc terrane are somewhat older (ca. 114–103 Ma) than the isolated intrusions within the basinal terrane (i.e., SRR-BRH intrusions) to the east (ca. 105–97 Ma) (Fig. 2). As defined in this study, GPS group magmatism (ca. 94–92 Ma) extends this range to a younger interval (i.e., ca. 105–92 Ma). Thus, the slightly younger intrusion ages within the basinal terrane suggest that the focus of arc magmatism may have shifted eastward into the back-arc region of northwestern Nevada during Early to Late Cretaceous time, coincident with the eastward migration and arc flare-up observed in the neighboring batholithic arc segments (i.e., Sierra Nevada and Idaho batholiths). This eastward shift in arc magmatism was accompanied by a minor NE-SW shortening event, well-preserved within the contact aureoles of mid-Cretaceous plutons of the northern

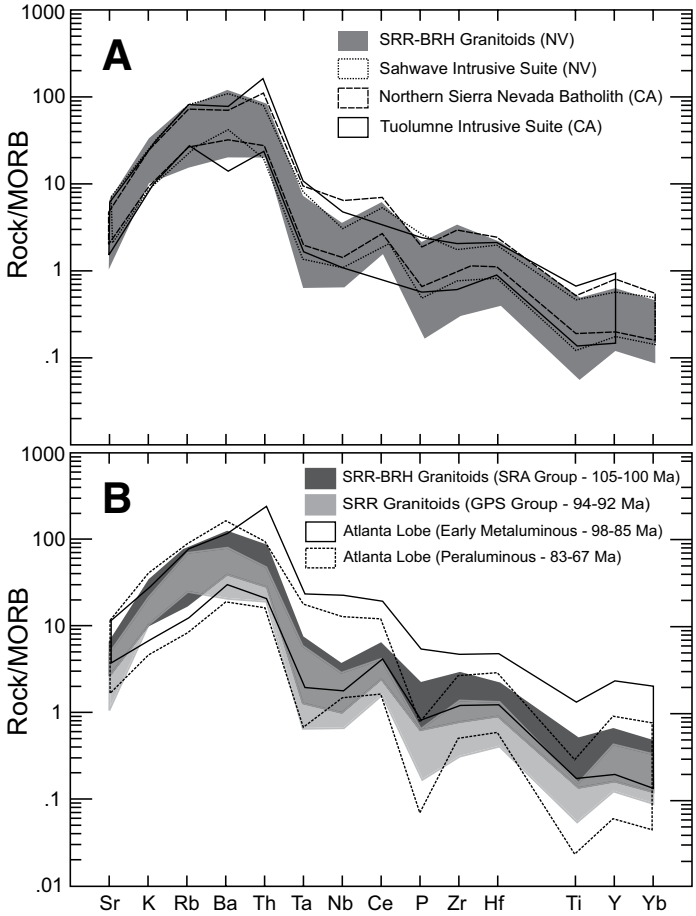

Figure 12. MORB-normalized trace element variation diagrams. Samples normalized to the values of Pearce (1983). (A) Comparison plot between the Santa Rosa Range and Bloody Run Hills (SRR-BRH) granitoids (dark gray shaded area) and the intrusive suites of California and western Nevada. The Sahwave Intrusive Suite (Van Buer and Miller, 2010); northern Sierra Nevada batholith (Cecil et al., 2012); Tuolumne Intrusive Suite (Gray et al., 2008). (B) Comparison plot between the SRR-BRH granitoids and Cretaceous intrusions of the Idaho batholith (Atlanta Lobe). The SRR-BRH granitoids are shown as the SRA (dark gray) and GPS (light gray) groups. Data for Idaho batholith from Gaschnig et al. (2011).

Luning-Fencemaker fold-and-thrust belt (Rogers, 1999; Wyld et al., 2001; Wyld, 2002; Ciavarella and Wyld, 2008). In the SRR, this shortening event is coeval with the timing of SRA group magmatism (Andorno stock, ca. 102 Ma; Wyld, et al., 2001; Wyld, 2002). Therefore, we argue that the similar emplacement ages (Fig. 11) and geochemical trends between the SRR-BRH intrusions and other arc segments (Fig. 12) support the continuity of the Late Cretaceous magmatic arc flare-up through northwestern Nevada and, in fact, bridge a gap between more westerly intrusions in northern Nevada and the Owyhee Mountains of southwestern Idaho.

CONCLUSIONS

The isolated intrusions of the SRR-BRH in northwestern Nevada are an excellent example of Cretaceous arc magmatism in the western Basin and Range Province. Field, petrographic, bulk geochemical, geochronologic, Sr and Nd isotope, and zircon Hf isotopic observations presented in this study better characterize magmatism in this region, placing these

intrusive suites into a broader regional context. The main conclusions identified within this study are as follows:

(1) The SRR-BRH contains two distinct granitoid suites/events: an older, more mafic and metaluminous suite (105–100 Ma, SRA group) and a younger, more felsic and peraluminous suite (94–92 Ma, GPS group). Although the SRA group is typical of granitoids emplaced in the basinal terrane of western and northwestern Nevada, the GPS group forms a small, but important, pulse of peraluminous magmatism not previously documented by earlier regional isotopic and structural studies.

(2) Al-in-hornblende thermobarometry reveal that the SRA group magmas were emplaced at paleodepths of ~5–10 km. Primary muscovite combined with prior structural and metamorphic contact aureole observations suggest slightly deeper emplacement for the GPS group magmas (~10.5–12 km). Consistent with previous emplacement estimates, these results confirm that the SRR-BRH intrusions represent shallow crustal magmatic systems.

(3) All of the SRR-BRH granitoids have bulk chemical signatures typical of subduction-related continental arc magmas. These intrusions also have bulk compositions similar to other Late Cretaceous arc granitoid suites within the North American Cordillera, providing evidence for the continuity of the Mesozoic magmatic arc through northwestern Nevada.

(4) Coupled with petrographic and geochemical observations, new U-Pb zircon geochronology documents that arc magmatism within this region shifted from metaluminous, mafic-intermediate compositions to more peraluminous, felsic compositions during Cretaceous time.

(5) Coincident with the observed shift in bulk composition, whole-rock Sr and Nd isotope and zircon Hf isotope data demonstrate that the relative crust/mantle contributions varied systematically with time, revealing a progressive shift from mantle-dominated magmas to magmas requiring more input from aged crustal reservoirs.

(6) The observed range of zircon Hf isotope compositions and U-Pb ages within xenocrystic zircon cores are strikingly similar to the detrital zircon record, namely the Triassic Osobb and Chinle Formations of Nevada and Utah. These data suggest that local metasedimentary units represent potential crustal inputs into the SRR-BRH magmatic systems.

Collectively, these observations and conclusions emphasize the importance of the isolated intrusions in northwestern Nevada in understanding the tectonomagmatic development and architecture of the Mesozoic continental margin. Despite being emplaced in fundamentally different lithospheric environments, the SRR-BRH intrusions share similar geochemical and isotopic patterns to the Sierra Nevada and Idaho batholiths, which were formed along and through thick North American lithosphere. This suggests some level of commonality in the sources and processes responsible for magma genesis along the entire (ca. 110–85 Ma) Cretaceous arc.

ACKNOWLEDGMENTS

We thank John Morton and Dave Kuentz (Miami University) for their laboratory assistance; Stan Mertzman (Franklin and Marshall College) for XRF analyses; and Chusi Li for assistance with the electron microprobe facilities at Indiana University. We also thank George Gehrels, Mark Pecha, and the staff at the Arizona Laserchron Center for assistance with U-Pb and Hf zircon isotope analyses (National Science Foundation support of the Laserchron Center, NSF-EAR 1338583). We also thank Dave Moecher, Claire McLeod, Calvin Miller, and two additional reviewers for their critical comments and suggestions that helped improve earlier versions of this manuscript. The U.S. Forest Service (Humboldt-Toiyabe National Forest and Santa Rosa Ranger Station) is acknowledged for providing a permit for sample collection within the Santa Rosa–Paradise Peak Wilderness during the initial 1990 field season (MS work of R. Stuck) and for logistical assistance. This work was supported by graduate student funding from the Geological Society of America, Sigma Xi, and Miami University to Brown. Hart acknowledges the support of the Janet and Elliot Baines Professorship and the National Science Foundation (NSF-EAR-0506887).

REFERENCES CITED

Amato, C.R., 1998, Progressive evolution of metamorphic differentiation preserved in a contact aureole [M.S. thesis]: Bloomington, Indiana University, 82 p.

Anderson, J.L., 1996, Status of thermobarometry in granitic batholiths: Earth and Environmental Science Transactions of the Royal Society of Edinburgh: v. 87, no. 1-2, p. 125–138, https://doi.org/10.1017/S0263593300006544.

Anderson, J.L., Barth, A.P., Wooden, J.L., and Mazdab, F., 2008, Thermometers and thermobarometers in granitic systems, *in* Putirka, K.D., and Tepley III, F. J., eds., Minerals, Inclusions, and Volcanic Processes: Reviews in Mineralogy and Geochemistry, v. 69, p.121–142, https://doi.org/10.2138/rmg.2008.69.4.

Anderson, J.L., and Smith, D.R., 1995, The effect of temperature and oxygen fugacity on Al-in- hornblende barometry: The American Mineralogist, v. 80, p. 549–559, https://doi.org/10.2138/am-1995-5-614.

Arehart, G.B., DeYoung, S., Poulson, S.R., Heaton, J.S., and Weiss, S., 2013, Sulfur isotopes in plutonic rocks of the Great Basin as indicators of crustal architecture: The Journal of Geology, v. 121, no. 4, p. 355–369, https://doi.org/10.1086/670651.

Armstrong, R.L., Taubeneck, W.P., and Hales, P.O., 1977, Rb-Sr and K-Ar geochronology of Mesozoic granitic rocks and their Sr isotopic compositions, Oregon, Washington, and Idaho: Geological Society of America Bulletin, v. 88, p. 397–411, https://doi.org/10.1130/0016-7606(1977)88<397:RAKGOM>2.0.CO;2.

Barton, M.D., Battles, D.A., Debout, C.E., Capo, R.C., Christensen, J.N., Davis, S.R., Hanson, R.B., Michelson, C.J., and Trim, H.G., 1988, Mesozoic contact metamorphism in the western United States, *in* Ernst, W.G., ed., Metamorphism and Crustal Evolution of the Western United States, Rubey Volume 7: Englewood Cliffs, New Jersey, Prentice Hall, p. 110–178.

Bateman, P.C., 1992, Plutonism in the central part of the Sierra Nevada batholith, California: U.S. Geological Survey Professional Paper 1483, 186 p.

Bateman, P.C., and Chappell, B.W., 1979, Crystallization, fractionation, and solidification of the Tuolumne Intrusive Series, Yosemite National Park, California: Geological Society of America Bulletin, v. 90, p. 465–482, https://doi.org/10.1130/0016-7606(1979)90<465:CFASOT>2.0.CO;2.

Benford, B., Crowley, J., Schmitz, M., Northrup, C.J., and Tikoff, B., 2010, Mesozoic magmatism and deformation in the northern Owyhee Mountains, Idaho: Implications for along-zone variations for the western Idaho shear zone: Lithosphere, v. 2, p. 93–118, https://doi.org/10.1130/L76.1.

Brown, K.L., and Hart, W.K., 2013, Late Cretaceous arc flare-up in northwestern Nevada: Elemental, zircon Hf, and U-Pb zircon geochronology of the Santa Rosa Range and Bloody Run Hills granitoids [Cordilleran section]: Geological Society of America Abstracts with Programs, v. 45, no. 6, p. 12.

Brown, K.L., Stuck, R., and Hart, W.K., 2010, Geochronology and geochemistry of a Late Cretaceous granitoid suite, Santa Rosa Range, Nevada: Linking arc magmatism in northwestern Nevada to the Sierra Nevada batholith [abs.]: Abstract V23B-2445 presented at 2010 Fall Meeting, AGU, San Francisco, California, 13-17 December, http://abstractsearch.agu.org/meetings/2010/FM/V23B-2445.html.

Brown, K.L., Stuck, R., and Hart, W.K., 2011, Geochemical heterogeneities along a paleocontinental margin: An example from the Late Cretaceous intrusions from the Santa Rosa Range, northwestern, Nevada: Geological Society of America Abstracts with Programs, v. 43, no. 5, p. 90.

Brueseke, M.E., and Hart, W.K., 2008, Geology and petrology of the mid-Miocene Santa Rosa-Calico volcanic field, northern Nevada: Nevada Bureau of Mines and Geology Bulletin 113, 82 p., http://www.nbmg.unr.edu/dox/dox.htm (accessed January 2018).

Brueseke, M.E., and Hart, W.K., 2009, Intermediate composition magma production in an intracontinental setting: Unusual andesites and dacites of the mid-Miocene Santa Rosa-Calico volcanic field, northern Nevada: Journal of Volcanology and Geothermal Research, v. 188, p. 197–213, https://doi.org/10.1016/j.jvolgeores.2008.12.015.

Brueseke, M.E., Heizler, M.T., Hart, W.K., and Mertzman, S.A., 2007, Distribution and geochronology of Oregon Plateau (U.S.A.) flood basalt volcanism: The Steens Basalt revisited: Journal of Volcanology and Geothermal Research, v. 161, p. 187–214, https://doi.org/10.1016/j.jvolgeores.2006.12.004.

Brueseke, M.E., Hart, W.K., and Heizler, M.T., 2008, Diverse mid-Miocene silicic volcanism associated with the Yellowstone-Newberry thermal anomaly: Bulletin of Volcanology, v. 70, p. 343–360, https://doi.org/10.1007/s00445-007-0142-5.

Camp, V.E., Ross, M.E., Duncan, R.A., Jarboe, N.A., Coe, R.S., Hanan, B.B., and Johnson, J.A., 2013, The Steens Basalt: Earliest lavas of the Columbia River Basalt Group, *in* Reidel, S.P., Camp, V.E., Ross, M.E., Wolff, J.A., Martin, B.S., Tolan, T.L., and Wells, R.E., eds., The Columbia River Flood Basalt Province: Geological Society of America Special Paper 497, p. 87–116, https://doi.org/10.1130/2013.2497(04).

Carlson, R.W., and Hart, W.K., 1988, Flood basalt volcanism in the northwestern United States, *in* Macdougall, J.D., ed., Continental Flood Basalts: The Netherlands, Kluwer Academic Publishers, p. 35–61, https://doi.org/10.1007/978-94-015-7805-9_2.

Cecil, M.R., Gehrels, G.E., Ducea, M.N., and Patchett, J., 2011, U-Pb-Hf characterization of the central Coast Mountains batholith: Implications for petrogenesis and crustal architecture: Lithosphere, v. 3, p. 247–260, https://doi.org/10.1130/L134.1.

Cecil, M.R., Rotberg, G.L., Ducea, M.N., Saleeby, J.B., and Gehrels, G.E., 2012, Magmatic growth and batholithic root development in the northern Sierra Nevada, California: Geosphere, v. 8, no. 3, p. 592–606, https://doi.org/10.1130/GES00729.1.

Ciavarella, V., and Wyld, S.J., 2008, Wall rocks as recorders of multiple pluton emplacement mechanisms: Examples from Cretaceous intrusions of northwest Nevada, *in* Wright, J.E., and Shervais, J.W., eds., Ophiolites, Arcs, and Batholiths: A Tribute to Cliff Hopson: Geological Society of America Special Paper 438, p. 1–34, https://doi.org/10.1130/2008.2438(19).

Colgan, J.P., Dumitru, T.A., Reiners, P.W., Wooden, J.L., and Miller, E.L., 2006, Cenozoic tectonic evolution of the Basin and Range Province in northwestern Nevada: American Journal of Science, v. 306, p. 616–654, https://doi.org/10.2475/08.2006.02.

Coleman, D.S., Gray, W., and Glazner, A.F., 2004, Rethinking the emplacement and evolution of zoned plutons: Geochronologic evidence for incremental assembly of the Tuolumne Intrusive Suite, California: Geology, v. 32, no. 5, p. 433–436, https://doi.org/10.1130/G20220.1.

Coleman, D.S., and Glazner, A.F., 1997, The Sierra Crest magmatic event: Rapid formation of juvenile crust during the Late Cretaceous in California: International Geology Review, v. 39, p. 768–787, https://doi.org/10.1080/00206819709465302.

Compton, R.R., 1960, Contact metamorphism in the Santa Rosa Range, Nevada: Geological Society of America Bulletin, v. 71, p. 1383–1416, https://doi.org/10.1130/0016-7606(1960)71[1383:CMISRR]2.0.CO;2.

DeCelles, P.G., 2004, Late Jurassic to Eocene evolution of the Cordilleran thrust belt and foreland basin system, western U.S.A.: American Journal of Science, v. 304, p. 105–168, https://doi.org/10.2475/ajs.304.2.105.

du Bray, E.A., 2007, Time, space, and composition relations among northern Nevada intrusive rocks and their metallogenic implications: Geosphere, v. 3, no. 5, p. 381–405, https://doi.org/10.1130/GES00109.1.

Ducea, M.N., Paterson, S.R., and DeCelles, P.G., 2015a, High-volume magmatic events in subduction systems: Elements, v. 11, no. 2, p. 99–104, https://doi.org/10.2113/gselements.11.2.99.

Ducea, M.N., Saleeby, J.B., and Bergantz, G., 2015b, The architecture, chemistry, and evolution of continental magmatic arcs: Annual Review of Earth and Planetary Sciences, v. 43, p. 299–331, https://doi.org/10.1146/annurev-earth-060614-105049.

Elison, M.W., and Speed, R.C., 1989, Structural development during flysch basin collapse: The Fencemaker allochthon, East Range, Nevada: Journal of Structural Geology, v. 11, p. 523–538, https://doi.org/10.1016/0191-8141(89)90085-0.

Elison, M.W., Speed, R.C., and Kistler, R.W., 1990, Geologic and isotopic constraints on the crustal structure of the northern Great Basin: Geological Society of America Bulletin, v. 102, p. 1077–1092, https://doi.org/10.1130/0016-7606(1990)102<1077:GAICOT>2.3.CO;2.

Farmer, G.L., and DePaolo, D.J., 1983, Origin of Mesozoic and Tertiary granite in the western United States and implications for pre-Mesozoic crustal structure 1: Nd and Sr isotopic studies in the geocline of the Northern Great Basin: Journal of Geophysical Research, v. 88, no. B4, p. 3379–3401, https://doi.org/10.1029/JB088iB04p03379.

Frost, B.R., Barnes, C.G., Collins, W.J., Arculus, R.J., Ellis, D.J., and Frost, C.D., 2001, A geochemical classification for granitic rocks: Journal of Petrology, v. 42, no. 11, p. 2033–2048, https://doi.org/10.1093/petrology/42.11.2033.

Gaschnig, R.M., Vervoort, J.D., Lewis, R.S., and McClelland, W.C., 2010, Migrating magmatism in the northern US Cordillera: In-situ U-Pb geochronology of the Idaho batholith: Contributions to Mineralogy and Petrology, v. 159, p. 863–883, https://doi.org/10.1007/s00410-009-0459-5.

Gaschnig, R.M., Vervoort, J.D., Lewis, R.S., and Tikoff, B., 2011, Isotopic evolution of the Idaho batholith and Challis intrusive province, northern US Cordillera: Journal of Petrology, v. 52, no. 12, p. 2397–2429, https://doi.org/10.1093/petrology/egr050.

Gaschnig, R.M., Vervoort, J.D., Tikoff, B., and Lewis, R.S., 2017, Construction and preservation of batholiths in the northern U.S. Cordillera: Lithosphere, v. 9, no. 2, p. 315–324, https://doi.org/10.1130/L497.1.

Gehrels, G.E., and Pecha, M., 2014, Detrital zircon U-Pb geochronology and Hf isotope geochemistry of Paleozoic and Triassic passive margin strata for western North America: Geosphere, v. 10, p. 49–65, https://doi.org/10.1130/GES00889.1.

Gehrels, G.E., Valencia, V., and Ruiz, J., 2008, Enhanced precision, accuracy, efficiency, and spatial resolution of U-Pb ages by laser ablation-multicollector-inductively coupled plasma-mass spectrometry: Geochemistry Geophysics Geosystems, v. 9, Q03017, https://doi.org/10.1029/2007GC001805.

Gehrels, G., Rusmore, M., Woodsworth, G., Crawford, M., Andronicos, C., Hollister, L., Patchett, J., Ducea, M., Klepeis, K., Friedman, D.R., Haggart, J., Mahoney, B., Crawford, W., Pearson, D., and Girardi, J., 2009, U-Th-Pb geochronology of the Coast Mountains batholith in northern-coastal British Columbia: Constraints on age and tectonic evolution: Geological Society of America Bulletin, v. 121, no. 9–10, p. 1341–1361, https://doi.org/10.1130/B26404.1.

Giorgis, S., McClelland, W., Fayon, A., Singer, B., and Tikoff, B., 2008, Timing of deformation and exhumation in the western Idaho shear zone, McCall, Idaho: Geological Society of America Bulletin, v. 120, no. 9–10, p. 1119–1133, https://doi.org/10.1130/B26291.1.

Grauch, V.J.S., Rodriquez, B.D., and Wooden, J.L., 2003, Geophysical and isotopic constraints on crustal structure related to mineral trends in north-central Nevada and implications for tectonic history: Economic Geology and the Bulletin of the Society of Economic Geologists, v. 98, p. 269–286.

Gray, W., Glazner, A.F., Coleman, D.S., and Bartley, J.M., 2008, Long-term geochemical variability of the Late Cretaceous Tuolumne intrusive suite, central Sierra Nevada, California, *in* Annen, C., and Zellmer, G.F., eds., Dynamics of Crustal Magma Transfer, Storage, and Differentiation: Geological Society of London Special Publication 304, p. 183–201, https://doi.org/10.1144/SP304.10.

Holland, T., and Blundy, J., 1994, Non-ideal interactions in calcic amphiboles and their bearing on amphibole-plagioclase thermometry: Contributions to Mineralogy and Petrology, v. 116, p. 433–447, https://doi.org/10.1007/BF00310910.

Hyndman, D.W., 1983, The Idaho batholith and associated plutons, Idaho and western Montana, *in* Roddick, J. A., ed., Circum-Pacific Plutonic Terranes: Geological Society of America Memoir 159, p. 213–240, https://doi.org/10.1130/MEM159-p213.

King, E.M., Valley, J.W., Stocki, D.F., and Wright, J.E., 2004, Oxygen isotope trends of granitic magmatism in the Great Basin: Location of the Precambrian craton boundary as reflected in zircons: Geological Society of America Bulletin, v. 116, p. 451–462, https://doi.org/10.1130/B25324.1.

Kistler, R.W., 1990, Two different lithosphere types in the Sierra Nevada, California, *in* Anderson, J.L., ed., The nature and origin of Cordilleran magmatism: Geological Society of America Memoir 174, p. 271–282, https://doi.org/10.1130/MEM174-p271.

Kistler, R.W., and Peterman, Z.E., 1978, Reconstruction of crustal blocks of California on the basis of initial strontium isotopic compositions of Mesozoic granitic rocks: U.S. Geological Survey Professional Paper 1071, 17 p.

Kistler, R.W., Evernden, J.F., and Shaw, H.R., 1971, Sierra Nevada plutonic cycle: Part I, origin of composite granitic batholiths: Geological Society of America Bulletin, v. 82, p. 853–868, https://doi.org/10.1130/0016-7606(1971)82[853:SNPCPI]2.0.CO;2.

Lackey, J.S., Valley, J.W., and Saleeby, J.B., 2005, Supracrustal input to magmas in the deep crust of Sierra Nevada batholith: Evidence from high-$\delta^{18}O$ zircon: Earth and Planetary Science Letters, v. 235, p. 315–330, https://doi.org/10.1016/j.epsl.2005.04.003.

Lackey, J.S., Cecil, M.R., Windham, C.J., Frazer, R.E., Bindeman, I.N., and Gehrels, G.E., 2012, The Fine Gold Intrusive Suite: The roles of basement terranes and magma source development in the Early Cretaceous Sierra Nevada batholith: Geosphere, v. 8, no. 2, p. 292–313, https://doi.org/10.1130/GES00745.1.

Lerch, D.W., Klemperer, S.L., Glen, J.M.G., Ponce, D.A., Miller, E.L., and Colgan, J.P., 2007, Crustal structure of the northwestern Basin and Range Province and its transition to unextended volcanic plateaus: Geochemistry Geophysics Geosystems, v. 8, no. 2, 21 p., https://doi.org/10.1029/2006GC001429.

Ludwig, K.R., 2008, User's manual for Isoplot 3.6: A geochronological toolkit for Microsoft Excel: Berkeley Geochronology Center Special Publication 4, 77 p.

Maffei, L., 1992, Petrogenesis of staurolite in K-poor metapelites of the Santa Rosa Range contact aureoles, Nevada [M.S. thesis]: Seattle, Washington, University of Washington, 83 p.

Martin, A.J., Wyld, S.J., Wright, J.E., and Bradford, J.H., 2010, The Lower Cretaceous King Lear Formation, northwest Nevada: Implications for Mesozoic orogenesis in the western U.S. Cordillera: Geological Society of America Bulletin, v. 122, no. 3/4, p. 537–562, https://doi.org/10.1130/B26555.1.

McKee, E.H., Noble, D.C., and Silberman, M.L., 1970, Middle Miocene hiatus in volcanic activity in the Great Basin area of the western United States: Earth and Planetary Science Letters, v. 8, p. 93–96, https://doi.org/10.1016/0012-821X(70)90156-1.

Miller, C.F., and Bradfish, L.J., 1980, An inner Cordilleran belt of muscovite-bearing plutons: Geology, v. 8, p. 412–416, https://doi.org/10.1130/0091-7613(1980)8<412:AICBOM>2.0.CO;2.

Miller, J.S., Matzel, J.E.P., Miller, C.F., Burgess, S.D., and Miller, R.D., 2007, Zircon growth and recycling during the assembly of large, composite arc plutons: Journal of Volcanology and Geothermal Research, v. 167, p. 282–299, https://doi.org/10.1016/j.jvolgeores.2007.04.019.

Miyashiro, A., 1974, Volcanic rock series in island arcs and active continental margins: American Journal of Science, v. 274, p. 321–355, https://doi.org/10.2475/ajs.274.4.321.

Morton, D.M., Miller, F.K., Kistler, R.W., Premo, W.R., Lee, C.T.A., Langenheim, V.E., Wooden, J.L., and Snee, L.W., 2014, Framework and petrogenesis of the northern Peninsular Ranges batholith, southern California, *in* Morton, D.M., and Miller, F.K., eds., Peninsular Ranges Batholith, Baja California and Southern California: Geological Society of America Memoir 211, p. 61–143, https://doi.org/10.1130/2014.1211(03).

Oldow, J.S., 1984, Evolution of a late Mesozoic back-arc fold and thrust belt, northwestern Great Basin, U.S.A.: Tectonophysics, v. 102, p. 245–274, https://doi.org/10.1016/0040-1951(84)90016-7.

Paterson, S.R., and Ducea, M.N., 2015, Arc magmatic tempos: Gathering the evidence: Elements, v. 11, no. 2, p. 91–98, https://doi.org/10.2113/gselements.11.2.91.

Pearce, J.A., 1983, Role of the sub-continental lithosphere in magma genesis at active continental margins, *in* Hawkesworth, C.J., and Norry, M.J., eds., Continental Basalts and Mantle Xenoliths: Nantwich, Shiva Publications, p. 230–249.

Pearce, J.A., Harris, N.B.W., and Tindle, A.G., 1984, Trace element discrimination diagrams for the tectonic interpretation of granitic rocks: Journal of Petrology, v. 25, p. 956–983, https://doi.org/10.1093/petrology/25.4.956.

Purcell, R.M., Brown, K.L., Hart, W.K., 2012, Petrology and geochemistry of a basinal terrane metamorphic assemblage, Santa Rosa Range, Nevada: Implications for local Late Cretaceous magmatism: Geological Society of America Abstracts with Programs, v. 44, no. 5, p. 10.

Reidel, S.P., Camp, V.E., Tolan, T.L., Kauffman, J.D., and Garwood, D.L., 2013, Tectonic evolution of the Columbia River flood basalt province, *in* Reidel, S.P., Camp, V.E., Ross, M.E., Wolff, J.A., Martin, B.S., Tolan, T.L., and Wells, R.E., eds., The Columbia River Flood Basalt Province: Geological Society of America Special Paper 497, p. 293–324, https://doi.org/10.1130/2013.2497(12).

Rogers, J.W., 1999, Jurassic-Cretaceous deformation in the Santa Rosa Range, Nevada: Implications for the development of the northern Luning-Fencemaker fold-and-thrust belt [M.S. thesis]: Athens, Georgia, University of Georgia, 195 p.

Shand, S.J., 1969, Eruptive Rocks: Their Genesis, Composition, Classification, and Their Relation to Ore-Deposits: New York, Hafner Publishing, 488 p.

Smith, J.G., McKee, E.H., Tatlock, D.B., and Marvin, R.F., 1971, Mesozoic granitic rocks in northwestern Nevada: A link between the Sierra Nevada and Idaho batholiths: Geological Society of America Bulletin, v. 82, p. 2933–2944, https://doi.org/10.1130/0016-7606(1971)82[2933:MGRINN]2.0.CO;2.

Solomon, G.C., and Taylor, H.P., Jr., 1989, Isotopic evidence for the origin of Mesozoic and Cenozoic granitic plutons in the northern Great Basin: Geology, v. 17, p. 591–594, https://doi.org/10.1130/0091-7613(1989)017<0591:IEFTOO>2.3.CO;2.

Speed, R.C., 1978, Paleogeographic and plate tectonic evolution of the early Mesozoic marine province of the western Great Basin, *in* Howell, D.G., and McDougall, K.A., eds., Mesozoic paleogeography of the western U.S.: Los Angeles, Pacific Section, Society of Economic Paleontologists and Mineralogists, Pacific Coast Paleogeography Symposium 2, p. 253–270.

Stewart, J.H., 1980, Geology of Nevada: Nevada Bureau of Mines and Geology Special Publication 4, 136 p.

Streckeisen, A., 1976, To each plutonic rock its proper name: Earth-Science Reviews, v. 12, p. 1–33, https://doi.org/10.1016/0012-8252(76)90052-0.

Stuck, R.J., 1993, Petrology and geochemistry of a Late Cretaceous granitoid suite, Santa Rosa mountain range, Humboldt County, Nevada [M.S thesis]: Oxford, Ohio, Miami University, 179 p.

Van Buer, N., and Miller, E., 2010, Sahwave batholith, NW Nevada: Cretaceous arc flare-up in a basinal terrane: Lithosphere, v. 2, no. 6, p. 423–446, https://doi.org/10.1130/L105.1.

Van Buer, N., Miller, E., and Dumitru, T.A., 2009, Early Tertiary paleogeologic map of the northern Sierra Nevada batholith and the northwestern Basin and Range: Geology, v. 37, p. 371–374, https://doi.org/10.1130/G25448A.1.

Watson, E.B., and Harrison, T.M., 1983, Zircon saturation revisited: Temperature and composition effects in a variety of crustal magma types: Earth and Planetary Science Letters, v. 64, p. 295–304, https://doi.org/10.1016/0012-821X(83)90211-X.

Wiswall, C.G., and Hyndman, D.W., 1987, Emplacement of the main plutons of the Bitterroot lobe of the Idaho batholith, *in* Vallier, T. L. and Brooks, H. C., eds., Geology of the Blue Mountains Region of Oregon, Idaho, and Washington: The Idaho batholith and its border zone: U. S. Geological Survey Professional Paper 1436, p. 59–72.

Wooden, J.L., Kistler, R.W., and Tosdal, R.M., 1998, Pb isotopic mapping of crustal structure in the northern Great Basin and relationships to Au deposit trends, *in* Tosdal, R.M., ed., Contributions to the gold and metallogeny of northern Nevada: U.S. Geological Survey Open-File Report 98-338, 290 p.

Wooden, J.L., Kistler, R.W., and Tosdal, R.M., 1999, Strontium, lead, and oxygen isotopic data for granitoids and volcanic rocks from the northern Great Basin and Sierra Nevada, California, Nevada, and Utah: U.S. Geological Survey, Open-File Report 99-569, 20 p.

Wright, J.E., and Wooden, J.L., 1991, New Sr, Nd, and Pb isotopic data from plutons in the northern Great Basin: Implications for crustal structure and granite petrogenesis in the hinterland of the Sevier thrust belt: Geology, v. 19, p. 457–460, https://doi.org/10.1130/0091-7613(1991)019<0457:NSNAPI>2.3.CO;2.

Wyld, S.J., 2000, Triassic evolution of the arc and back-arc of northwest Nevada, and evidence for extensional tectonism, *in* Soreghan, M.J., and G.E., Gehrels, eds., Paleozoic and Triassic paleogeography and tectonics of western Nevada and northern California: Geological Society of America Special Paper 347, p. 185–207.

Wyld, S.J., 2002, Structural evolution of a Mesozoic backarc fold-and-thrust belt in the U.S. Cordillera: New evidence from northern Nevada: Geological Society of America Bulletin, v. 114, no. 11, p. 1452–1468, https://doi.org/10.1130/0016-7606(2002)114<1452:SEOAMB>2.0.CO;2.

Wyld, S.J., and Wright, J.E., 2000, Timing of deformation in the Mesozoic Luning-Fencemaker fold-thrust belt, Nevada: Geological Society of America Abstracts with Programs, v. 32, no. 7, p. A169–A170.

Wyld, S.J., and Wright, J.E., 2001, New evidence for Cretaceous strike-slip faulting in the United States Cordillera and implications for terrane-displacement, deformation patterns, and plutonism: American Journal of Science, v. 301, p. 150–181, https://doi.org/10.2475/ajs.301.2.150.

Wyld, S.J., and Wright, J.E., 2005, Early Cretaceous, margin-parallel, dextral faulting and terrane translation in the U.S. Cordillera: Geological Society of America Abstracts with Programs, v. 37, no. 4, p. 102.

Wyld, S.J., and Wright, J.E., 2009, Jurassic orogenesis in northwestern Nevada: Timing, kinematics and relations (if any?) to the Sevier Orogeny: Geological Society of America Abstracts with Programs, v. 41, no. 7, p. 588.

Wyld, S.J., Copeland, P., and Rogers, J.W., 1999, $^{40}Ar/^{39}Ar$ whole rock phyllite ages from the Mesozoic Luning-Fencemaker thrust belt of central Nevada: Eos, v. 80, no. 46, p. F977.

Wyld, S.J., Rogers, J.W., and Wright, J.E., 2001, Structural evolution within the Luning-Fencemaker fold-thrust belt, Nevada: Progression from back-arc basin collapse to intra-arc shortening: Journal of Structural Geology, v. 23, p. 1971–1995, https://doi.org/10.1016/S0191-8141(01)00042-6.

Wyld, S.J., Rogers, J.W., and Copeland, P., 2003, Metamorphic evolution of the Luning-Fencemaker fold-thrust belt, Nevada: Illite crystallinity, metamorphic petrology, and 40Ar/39Ar geochronology: The Journal of Geology, v. 111, p. 17–38, https://doi.org/10.1086/344663.

Zartman, R.E., 1974, Lead isotopic provinces in the Cordillera of the western United States and their geologic significance: Economic Geology and the Bulletin of the Society of Economic Geologists, v. 69, p. 792–805, https://doi.org/10.2113/gsecongeo.69.6.792.

MANUSCRIPT RECEIVED 7 AUGUST 2017
REVISED MANUSCRIPT RECEIVED 24 JANUARY 2018
MANUSCRIPT ACCEPTED 9 FEBRUARY 2018